STUDIES OF UNDERDOPED $La_{2-x}Ba_xCuO_4$ SINGLE CRYSTALS

X-ray and neutron scattering studies of underdoped $La_{2-x}Ba_xCuO_4$ single crystals

By

Yang Zhao, M. Eng. B. Sc.

A Thesis
Submitted to the School of Graduate Studies
in Partial Fulfillment of the Requirements
for the Degree
Doctor of Philosophy

McMaster University

Doctor of Philosophy (2008)
(Physics)

McMaster University
Hamilton, Ontario

TITLE: X-ray and neutron scattering studies of underdoped $La_{2-x}Ba_xCuO_4$ single crystals

AUTHOR: Yang Zhao, M. Eng., B. Sc. (Peking University)

SUPERVISOR: Dr. B. D. Gaulin

NUMBER OF PAGES: xi, 110

Abstract

The interplay between superconductivity, magnetism and crystal structure is a central issue in the study of the high T_c cuprates. The transition metal compound $La_{2-x}Ba_xCuO_4$ (LBCO) was the very first high T_c superconductor, discovered by J. G. Bednorz and K. A. Müller in 1986. However, it has been much less extensively studied than other high T_c materials, due to the difficulty of growing large single crystals. With our Image Furnace facility, we have successfully grown high quality, large LBCO crystals (with $x \sim 0.095$, 0.08, 0.05 and 0.025) on the underdoped side of the well known 1/8 ($x=0.125$) anomaly in this material's phase diagram.

Using our rotating anode X-ray source at McMaster University, we have performed high-resolution X-ray diffraction studies on our $x=0.095$ and 0.08 samples and on a 1/8 doped LBCO ($x=0.125$) crystal grown by our collaborators. The X-ray study mapped out a sequence of tetragonal and orthorhombic crystal structures with temperature, which were known from earlier measurements.

We have also performed neutron scattering studies at several Laboratories on x=0.095, 0.08, 0.05 and 0.025 samples. We observed elastic spin incommensurate Bragg peaks in all samples, and inelastic measurements on the x=0.095 sample allowed us to explore the material's low energy spin fluctuations. The elastic neutron scattering results of higher doped samples (x=0.095 and 0.08) indicate that "collinear" static incommensurate magnetic ordering develops below the low temperature structural phase transition, and this order persists into the superconducting state. Static incommensurate magnetic order is also observed in the $La_{2-x}Ba_xCuO_4$ (x=0.05 and 0.025) compounds with ordering wavevectors which are rotated by 45° about the commensurate (0.5,0.5,0) position, with respect to that in the superconducting x=0.095 and 0.08 samples. These spin modulations are one dimensional in the x=0.05 and 0.025 samples, with ordering wavevectors lying along the orthorhombic b^* direction. Such a rotation in the orientation of the static spin ordering as a function of increasing Ba doping, from diagonal to collinear, is roughly coincident with the transition from an insulating to a superconducting ground state and is similar to that observed in the related $La_{2-x}Sr_xCuO_4$ system. The low energy, inelastic neutron scattering studies show that the dynamic spin susceptibility for x=0.095 is constant within the superconducting state and decreases as the temperature rises above T_c.

Acknowledgements

First, I would like to sincerely thank my supervisor, Professor. Bruce D. Gaulin for his guidance, patience and encouragement throughout my Ph. D. study at McMaster. I would extend my thanks to Professor John. E. Greedan and Professor Graeme M. Luke for their assistance as members of my supervisor committee. In addition, I especially thank Dr. Hanna. A. Dabkowska and Dr. Antoni B. Dabkowska for their guidance during $La_{2-x}Ba_xCuO_4$ single crystal growth and characterization. I like to thank many students and postdocs for their help and friendship during my stay at McMaster, in particular, I deeply thank Dr. Sarah R. Dunsiger and Dr. John-Paul Castellan for their endless help and thoughtful discussion during this work. I also like to thank Marek Kiela for his technical support during X-ray experiment.

At Chalk River, NIST and LLB, my sincere thanks go to Dr. William J. L. Buyers, Dr. Zahra Yamani, Dr. John R. D. Copley, Dr. Yiming Qiu, Dr. Philippe Bourges and Dr. Yvan Sidis. Their hospitality and assistance make experiments very delightful. My thanks also go to Larry McEwan, Raymond Sammon and Mel Potter for their technical assistance during my visits at the laboratory. I have also benefited from many expertise and staffs not mentioned, but certainly not forgotten.

I would also like to acknowledge financial assistant from McMaster University.

Finally, I am greatly indebted to my family for their years of support and encouragement. I pay special thanks to my wife, Ting Xue for her understanding and love and our daughter Ruqing who provides me a source of pride.

Contents

List of Figures

List of Tables

Chapter 1

Introduction

1.1 General outline

The complex interplay among spin, charge, and lattice degrees of freedom in the quasi-two dimensional copper-oxide high temperature superconductors have been the subject of intense interest since the discovery of superconductivity in the $La_{2-x}Ba_xCuO_4$ system some 21 years ago (Bednorz and Müller, 1986). Both $La_{2-x}Ba_xCuO_4$ and $La_{2-x}Sr_xCuO_4$ display a fascinating series of structural, magnetic and superconducting phase transitions as a function of temperature (Kastner et al., 1998). While $La_{2-x}Ba_xCuO_4$ was the first layered cuprate high T_c superconductor to be discovered, difficulties associated with the growth of high quality single crystals have significantly limited its study. As a result the $La_{2-x}Ba_xCuO_4$ family is much less well studied than the $La_{2-x}Sr_xCuO_4$ family and other high temperature superconductor families which have an extended history of being grown and characterized in single crystal form (Kastner et al., 1998), such as the $YBa_2Cu_3O_{7-\delta}$ and $Bi_2Sr_2CaCu_2O_8$ families (Birgeneau et al., 2006; Eschrig, 2006; Fong et al., 1999; Castellan et al., 2006).

While the Sr and Ba doped La-214 compounds have much in common, there is a remarkable difference in their temperature-doping phase diagram. Both systems undergo a high temperature phase transition from a tetragonal to an orthorhombic crystal structure with decreasing temperature. Both systems also have an anomaly near 1/8-doping (x=0.125), but in the case of LBCO, the nature of the anomaly is that the superconducting transition temperature drops precipitously to ~1K from ~28 K for concentrations to either side of x=0.125. LSCO in contrast shows only a modest ~10% dip in Tc near this concentration. In LBCO, this anomaly is known to coincide with the appearance of a second low temperature tetragonal phase. This indicates the subtle role of the lattice in influencing the low temperature electronic properties and highlights the need to study both the Ba and Sr doped compounds.

This thesis reports significant progress made in single crystal growth of the Ba doped $La_{2-x}Ba_xCuO_4$ family and also in X-ray and neutron scattering studies using the resulting $La_{2-x}Ba_xCuO_4$ single crystals. The high resolution X-ray study focusses on a comparison between the structural and superconducting phase diagrams in polycrystalline and single crystal materials, critical phenomena associated with the High Temperature Tetragonal (HTT) phase → the Middle Temperature Orthorhombic (MTO) phase transition, and the nature of the Low Temperature Tetragonal (LTT) phase in x=0.125 and 0.095 samples at low temperatures. Neutron scattering studies concentrate on the evolution of magnetism in $La_{2-x}Ba_xCuO_4$ as a function of doping. Similar to underdoped $La_{2-x}Sr_xCuO_4$ system, elastic neutron scattering studies show incommensurate (IC) magnetic peaks which rotate by 45 degrees from along the *diagonal* direction to along the *collinear* direction as Ba doping increases.

This change is coincident with the transition from the spin glass regime to the superconducting regime in this system. Most of this work has been published in scientific journals (Zhao et al., 2007; Dunsiger et al., 2008a) or will be published in near future (Dunsiger et al., 2008b). Some completed work is not reported in this thesis. This work includes recent neutron scattering studies on very lightly doped $La_{2-x}Ba_xCuO_4$ (x=0.0125) single crystals.

The remainder of this chapter will briefly introduce the crystal structure and magnetic phase diagram of underdoped $La_{2-x}Ba_xCuO_4$ materials and will compare these results with corresponding results on $La_{2-x}Sr_xCuO_4$.

1.2 The crystal structure of $La_{2-x}Ba_xCuO_4$

Figure 1.1 a) shows the crystal structure of undoped La_2CuO_4. As can be seen, it contains two dimensional CuO_2 layers. The crystal structure is relatively simple compared with other high T_c cuprates such as $YBa_2Cu_3O_{7-\delta}$ or $Bi_2Sr_2CaCu_2O_8$. One of the many interesting properties of the $La_{2-x}Ba_xCuO_4$ family is the sequence of structural phase transitions which this material displays on cooling below room temperature for underdoped Ba concentrations ($x < 0.18$). As shown in figure 1.1 b), previous studies on polycrystalline $La_{2-x}Ba_xCuO_4$ shows three different structures, which proceed on cooling from the HTT phase (space group, $I4/mmm$), to the MTO phase (space group, $Bmab$) and finally to the LTT phase (space group, $P4_2/ncm$) (Axe et al., 1989a,b; Suzuki and Fujita, 1989a,b; Adachi et al., 2001). During the HTT to MTO phase transition, the unit cell of $La_{2-x}Ba_xCuO_4$ doubles, and the lattice parameter $a_{ortho} \approx \sqrt{2}a_{tetra}$. In the HTT phase, the $\vec{a}$ lattice parameter is directed along the nearest neighbor Cu-O-Cu direction with the value about

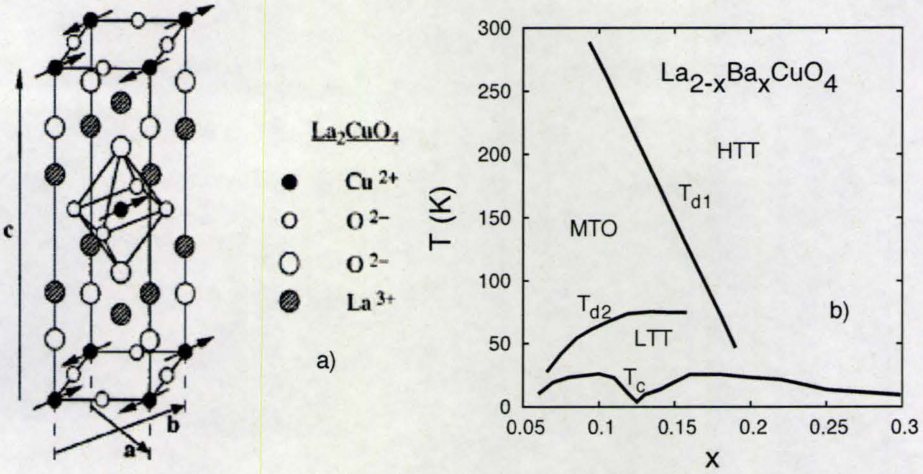

Figure 1.1: a) Crystal structure of undoped La_2CuO_4. Ba^{2+} replace La^{3+} in the $La_{2-x}Ba_xCuO_4$and introduces holes into CuO_2 plane. b) Phase diagram of $La_{2-x}Ba_xCuO_4$. T_{d1} and T_{d2} refer to two structure phase transitions and T_c is the superconducting transition temperature. The data used for this plot is based on Adachi *et al.* (Adachi et al., 2001) which reported on work using powder samples.

3.78Å. On the other hand, in the MTO and LTO phase, $\vec{a}$ and $\vec{b}$ point along next near neighbor Cu-Cu direction as shown in figure 1.1 a).

The HTT→MTO and the MTO→LTT phase transition temperatures are referred to as T_{d1} and T_{d2}, respectively. The HTT→MTO transition is continuous, while the MTO→LTT transition is known to be strongly discontinuous. These structures are closely coupled to the magnetic and electronic properties of the $La_{2-x}Ba_xCuO_4$ and $La_{2-x}Sr_xCuO_4$ families. The phase diagram of the $La_{2-x}Ba_xCuO_4$ system contains a dome of LTT phase, which is centred around x=0.125. This Ba-concentration corresponds to a steep depression of the superconducting T_C as a function of concentration, known as the 1/8 anomaly (Axe et al., 1989b; Moodenbaugh et al., 1988). The $La_{2-x}Sr_xCuO_4$ system shows a much smaller $\sim$ 10% dip in T_c at x=0.125 and the absence of the LTT phase at low temperatures (Nagano et al., 1993; Radaelli et al., 1994). The 1/8 anomaly within the LTT phase also corresponds to strong incommensurate magnetic long range order at temperatures just below the completion of the MTO-LTT phase transition (Fujita et al., 2004; Tranquada et al., 2004). Clearly, the structural, magnetic, and superconducting properties of the $La_{2-x}Ba_xCuO_4$ and $La_{2-x}Sr_xCuO_4$ systems are strongly coupled.

The critical phenomena associated with the HTT-MTO transition have been previously studied in undoped La_2CuO_4 as well as in $La_{2-x}Sr_xCuO_4$ in single crystal and polycrystal form (Birgeneau et al., 1987; Vaknin et al., 1987; Böni et al., 1988; Braden et al., 1994; Ting and Fossheim, 1993; Thurston et al., 1989), as single crystals of these materials have existed for some time. These studies show the HTT→MTO phase transition to be characterized with an order parameter critical exponent β varying from 0.28 to 0.37 (Birgeneau et al., 1987; Vaknin et al., 1987; Böni et al., 1988; Braden et al., 1994; Ting and

Fossheim, 1993; Thurston et al., 1989). Studies on polycrystalline samples of $La_{2-x}Ba_xCuO_4$ by Susuki *et al.* produced estimates for $\beta \sim 0.33$ (Suzuki and Fujita, 1989a,b), which are consistent with expectations for 3D universality (Collins, 1989).

1.3 Magnetic structure

Figure 1.1 a) also shows the magnetic structure appropriate to La_2CuO_4. Cu^{2+} has $3d^9$ electronic configuration. The one unpaired electron of Cu ion has a spin 1/2 and is coupled via antiferromagnetic exchange with the near neighbor Cu ions. Because of the strong Coulomb interaction, the unpaired electron localizes at each Cu site. La_2CuO_4 is a classical antiferromagetic Mott insulator with a Néel temperature T_N=325K. (Kastner et al., 1998) Previous neutron scattering study shows the magnetic structure in undoped La_2CuO_4(Vaknin et al., 1987) to be relatively simple two sublattice antiferromagnets characterized by a commensurate Bragg peak at (0.5, 0.5, 0), also refered to as (π, π), in reciprocal lattice units within the high temperature tetragonal basal plane.

When La_2CuO_4 is doped with Ba, the substitutional ion of Ba^{2+} for La^{3+} introduces holes in CuO_2 layers and severely disrupts the long range antiferromagnetic ordering. As a result, the commensurate Bragg peak at (0.5, 0.5, 0) splits into incommensurate magnetic peaks as illustrated in figure 1.2. The origin of the incommensurate magnetic structure as a function of doping in high T_c cuprates is still under debate.

One explanation for the origin of the incommensurate structure is the so called stripe phase model at low temperature in doped $La_{2-x}Ba_xCuO_4$ or $La_{2-x}Sr_xCuO_4$. Within the stripe picture of doped, two dimensional Mott

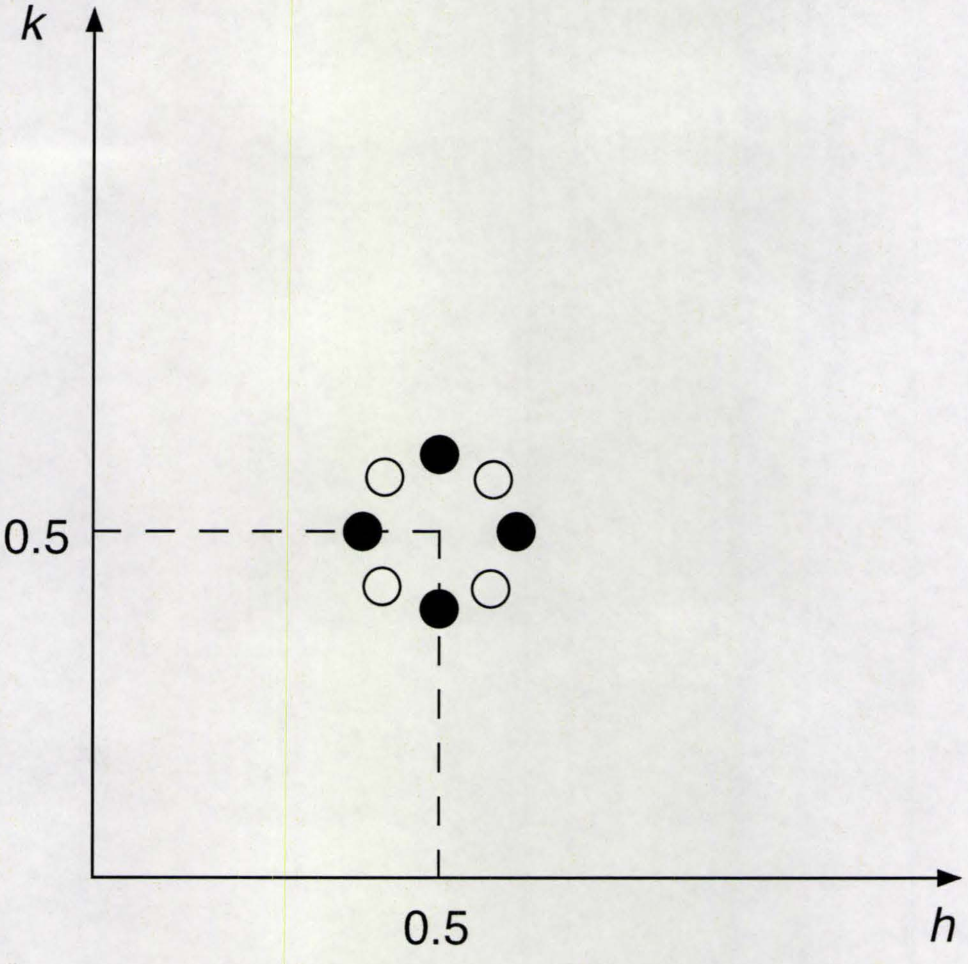

Figure 1.2: The schematic diagram of incommensurate magnetic peaks in $(h, k, 0)$ plane. The closed and open circles illustrate the collinear and diagonal splitting directions, respectively

insulators, the non-magnetic holes in these materials organize into quasi-one dimensional stripes which separate antiferromagnetic insulating antiphase domains (Kivelson et al., 2003). Adjacent antiferromagnetic regions are π out of phase with each other giving rise to a magnetic structure with incommensurate periodicity, where the supercell dimension is twice the hole stripe periodicity. This incommensurate magnetism has been carefully studied in $La_{2-x}Sr_xCuO_4$ system, where the incommensurate magnetism can be either static or dynamic, as evidenced by either elastic or inelastic peaks in the neutron scattering respectively and now appears to be a common feature of the $La_{2-x}Sr_xCuO_4$ family of compounds. Specifically, for lightly doped $La_{2-x}Sr_xCuO_4$, elastic incommensurate magnetic Bragg features first appear split off from the (0.5,0.5) position in diagonal directions relative to a tetragonal unit cell (Matsuda et al., 2000; Wakimoto et al., 2000). At higher doping in the underdoped superconducting regime, the peaks rotate by 45° to lie along directions parallel to the tetragonal axes or Cu-O-Cu bonds, such that elastic magnetic scattering appears at $(0.5\pm\delta,0.5,0)$ and $(0.5,0.5\pm\delta,0)$ (Kimura et al., 1999). For optimal and higher doping the static order disappears, but dynamic incommensurate correlations nevertheless persist (Kimura et al., 1999; Wakimoto et al., 2004).

Another interpretation for these incommensurate spin ordered states is spin-density-wave (SDW)ordering. SDW order was initially proposed to explain the slightly incommensurate antiferromagnetic ordering in elemental Cr (Fawcett, 1988), which is found to be similar to the magnetism observed in the cuprates. In the SDW model, the ordered magnetic state is described in terms of electron-hole pair excitations about an underlying Fermi surface (Norman and Pépin, 2003). The amplitude of the SDW order can be understood as originating from approximate nesting of separate electron and hole Fermi surfaces.

In Cr alloys, such an ordered state can be modified by adjusting the Fermi surface energy through the substitution of Cr with its neighbouring elements. The SDW wave vector can change from incommensurate to commensurate in Cr alloys. A comparison of the magnetic excitation spectrum in Cr alloys to that in high T_c cuprates reveals very similar phenomena and many people believe the similar mechanism might underly the complex magnetic ordering in superconducting cuprates.

Chapter 2

The crystal growth of underdoped $La_{2-x}Ba_xCuO_4$ single crystals

2.1 Introduction

In order to study the crystal and magnetic structure of $La_{2-x}Ba_xCuO_4$ system, we need grow the high quality single crystals with a variety of different doping levels. This chapter discusses the growth or large single crystals of $La_{2-x}Ba_xCuO_4$ using the traveling solvent floating zone technique. We have successfully grown large $La_{2-x}Ba_xCuO_4$ single crystals with several different doping levels. The range of our crystals covers compositions in the insulating spin-glass-like regime to the superconducting regime. More importantly, all single crystals grown are sufficiently large to be suitable for neutron scattering studies (see Chapter 5). The last section in this chapter also presents the susceptibility measurements of $La_{2-x}Ba_xCuO_4$ single crystals with different doping levels, which characterizes their bulk magnetic properties.

2.2 The traveling solvent floating zone method

The traveling solvent floating zone (TSFZ) method is an advanced single crystal growth technique. As shown in figure 2.1, the TSFZ method employs an optical image furnace system. It uses focused light to heat the materials. The optical image furnace contains the following parts: a) high power halogen lamps and precisely aligned focus mirrors, b) rotatable upper and lower shafts to support the feed and seed rods, c) quartz tube to enclose the growth environment. The optical image furnace system usually has two or four ellipsoidal mirrors and corresponding halogen lamps. Before the growth, a pre-annealed rod of starting material is hung on the upper shaft and used as a feed rod. Another pre-annealed rod or small crystal with same compound is attached to the lower shaft and employed as a seed rod. Depending on the materials, a small piece of the flux with similar composition to the starting material maybe needed at the beginning of the growth. During the crystal growth, the feed rod is translated through a hot zone produced by focussed light from the halogen light-bulbs, by either moving the shaft or the mirrors. The rod melts at the upper side of the zone and solidifies at the lower side. The temperature of molten zone is controlled by the DC power of halogen lamps. The feed and seed rods rotates in opposite direction to obtain a good mixing of the molten materials and a homogeneous heating of the molten zone. The growth environment is enclosed within the quartz tube in the presence of a specific gas at a specific pressures depending on the materials used.

With the TSFZ technique, the molten zone is kept in place by its surface

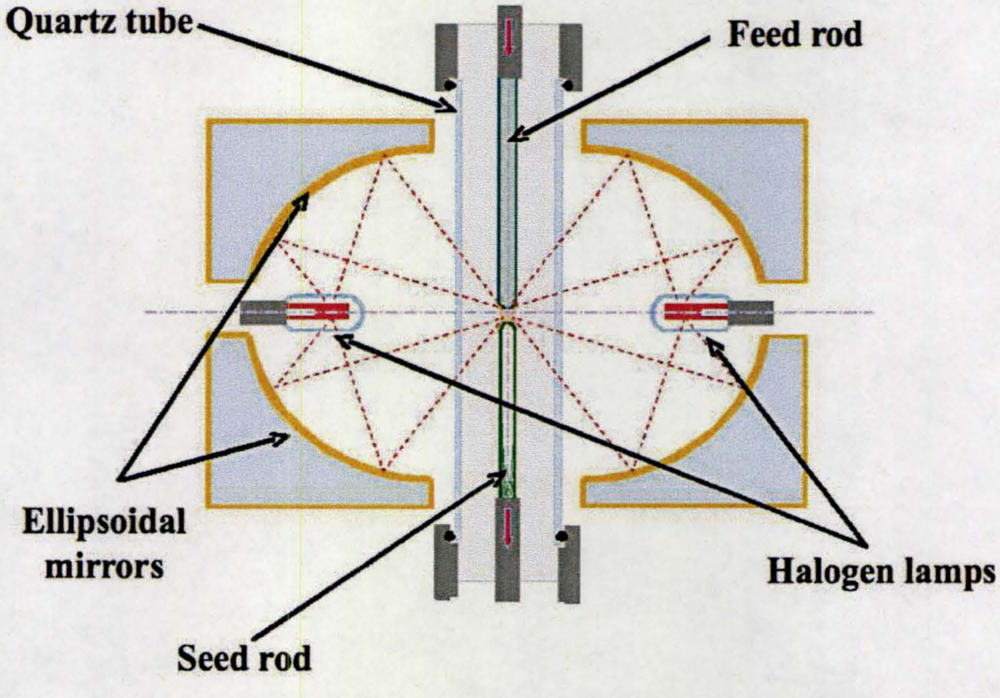

Figure 2.1: A schematic diagram for the TSFZ method.

tension and it has several advantages relative to other growth techniques. The most important advantage is that there is no contact between a container and the material of interest during the growth process. This means that a relatively contamination-free crystal can be produced. Furthermore, the molten zone travels through the feed rod, which means that the composition is continuously dissolved in the solvent and grown out of the solvent. If the doped feed rod is homogeneously distributed, the grown single crystal should be homogeneously doped. The TSFZ method can be used to grow large single crystals, which makes it particularly well suited to neutron scattering studies which require large volumes of sample for meaningful studies. There is no theoretical limit to the length of the crystals grown by the TSFZ method. In practice, the single crystals grown usually have typical dimensions of several centimeters long and 4 to 6 mm in the diameter. The diameter of single crystals is limited by the size of molten zone. However, the optimized growth condition is set by a variety of parameters such as the lamp power, the growth rate, the gas pressure and the rotation speed of both the feed and seed rods. Thus, the entire growth process is quite complex and can be very difficult to perform and optimize. In addition, the growth process can require several days due to a slow growth rate, which is always the case for high T_c superconductor materials.

2.3 The preparation of starting materials

We studied several high quality $La_{2-x}Ba_xCuO_4$ single crystals. During the course of this thesis, I will discuss single crystals with five different doping levels, that is specifically x=0.125, 0.095, 0.08, 0.05 and 0.025. All crystals were grown by using traveling solvent, floating zone image furnace techniques. The x=0.125 sample was grown separately, and the details of this growth have been previously discussed (Fujita et al., 2004; Tranquada et al., 2004).

All $La_{2-x}Ba_xCuO_4$ single crystal growths followed similar processes and procedures, and employed polycrystalline La_2O_3, $BaCO_3$ and CuO as starting materials to make the initial, polycrystalline feed rod and solvent. For the production of the feed rods, the starting materials were mixed in the proper ratio appropriate to each growth with the exception of the x=0.095 and 0.08. The x=0.095 and x=0.08 feed rods were prepared with starting materials at a ratio of La:Ba=1.875:0.125. These materials were mixed, ground, and annealed at 980°C for 12 hours in air. This process was repeated in order to ensure homogeneous feed rods. To compensate for Cu evaporation during the crystal growth, the pre-annealed feed rods were mixed with extra CuO. A further 1% to 2% mol CuO was added to the starting polycrystalline materials and thoroughly mixed to prepare the final feed rods. The final feed rods were heated to a temperature of 1190°C, at a rate of 100°C/hour. They were held at this temperature for 12 hours. We also employed a solvent, formed from the original polycrystalline feed rod, with CuO added so as to reach a final ratio of constituent atoms ($La_{2-x}Ba_x$):Cu=3:7 for each Ba concentration. After mixing and sintering, small disks of the solvent weighing ~ 0.4 g were cut out and used as solvents in the subsequent single crystal growths.

2.4 The single crystal growth

The single crystal growths were carried out using a four-mirror image furnace (Crystal System Inc.). Small La_2CuO_4 or $La_{2-x}Ba_xCuO_4$ single crystals were employed as the seed rod for all growths. All growth rate were 1mm/h with a counter-rotation speed of 25 rpm for both feed and seed rods. Each growth process took up to four days to complete. To achieve a successful growth, we examined several growth protocols and resulting optimized growth conditions are listed in table 2.1.

Table 2.1: Summary of single crystal growth conditions of $La_{2-x}Ba_xCuO_4$

x	Starting materials	Power	Rate	Gas and pressure
0.095	$La_{1.875}Ba_{0.125}CuO_4$ +1%CuO	77~ 79.1%	1mm/hour	O_2 165 kPa
0.08	$La_{1.875}Ba_{0.125}CuO_4$ +2%CuO	82~ 83%	1mm/hour	O_2 182 kPa
0.05	$La_{1.95}Ba_{0.05}CuO_4$ +1.5%CuO	77%	1mm/hour	extra dry O_2 182 kPa
0.025	$La_{1.975}Ba_{0.025}CuO_4$ +1.5%CuO	77%	1mm/hour	extra dry O_2 171 kPa

Upon completion of the growths, the as-grown single crystals were kept above 100°C in a furnace to prevent hydrolysis of the material, which is known to be problematic for single crystals of $La_{2-x}Ba_xCuO_4$. As shown in figure 2.2, all crystals had similar dimensions of 80 mm long by 5 mm in diameter as-grown. For the x=0.095 and 0.08 samples, within the first week following completion of the growths, the initial $\sim$ 30 mm of the single crystals turned to dust as a result of hydrolysis of a second phase. The undamaged part of all crystals was stable. These had approximate dimensions of 50 mm long by 5 mm in diameter for x=0.095 and 55 mm long by 5 mm in diameter for x=0.08. The lower doping crystals, x=0.05 and 0.025, were much more stable after growth due to lower Ba concentrations. These crystals were sufficiently large to allow for advanced characterization by neutron scattering techniques which will be discussed in more detail in Chapter 5 of this thesis.

It is worth making a special note regarding the x=0.095 and 0.08 samples. While these two crystal growths were initiated with similar starting materials, and the growths followed similar procedures, the Ba/La ratio, as identified by T_{d1} and T_{d2}, were different at the $\sim 15\%$ level, see Chapter 4. This originates from Cu evaporation during the growth. All the phase transitions observed (structural, magnetic, and superconducting) are nevertheless very sharp in temperature, indicating excellent homogeneity of concentration within the individual single crystals. The chemical analysis result of the x=0.095 sample shows different Ba concentration with x=0.075, however the result also gives a larger deviation. Based on the accurate measurements of T_{d1} on x=0.095 and 0.08 samples, which will be discussed in more detail in Chapter 4, we determined the doping levels of these two samples.

2.5 Single crystal characterization

After resulting single crystals were stabilized, the volume of the single crystals were cut into various sizes for different experiments. The largest piece was used for neutron scattering experiments, while small pieces cut from near the end of the crystal growth were used for X-ray and magnetization measurements. The growth direction mainly depends on the direction of the seed rods which were employed. For all the crystals, which will be discussed in this thesis, have growth directions along the (1,1,0) within HTT phase.

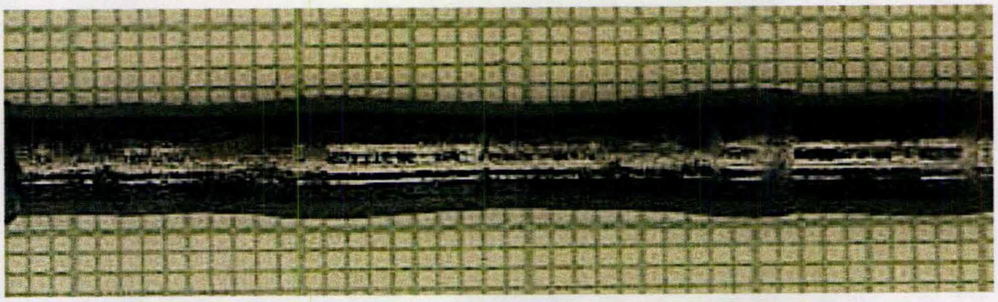

a) x=0.095

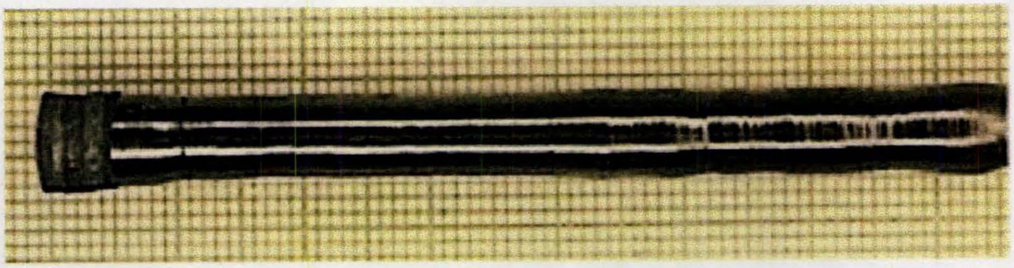

b) x=0.08

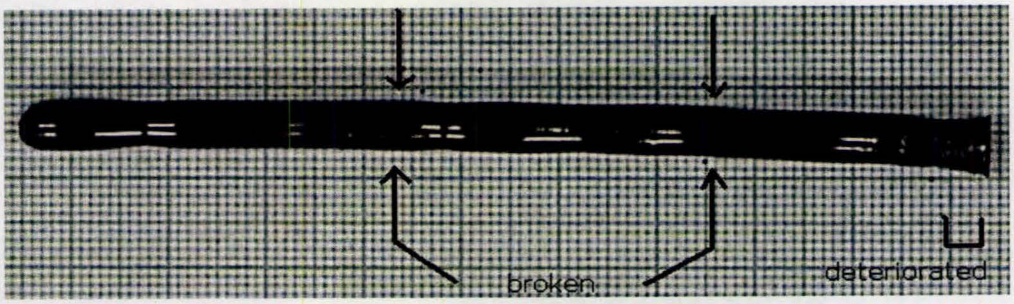

c) x=0.025

Figure 2.2: Some samples of as grown $La_{2-x}Ba_xCuO_4$ single crystals with doping levels a) x=0.095, b) x=0.08 and c) x=0.025. All crystals are grown using TSFZ method and have similar dimensions, $\sim$ 80 mm(L)× 5 mm(D), after growing.

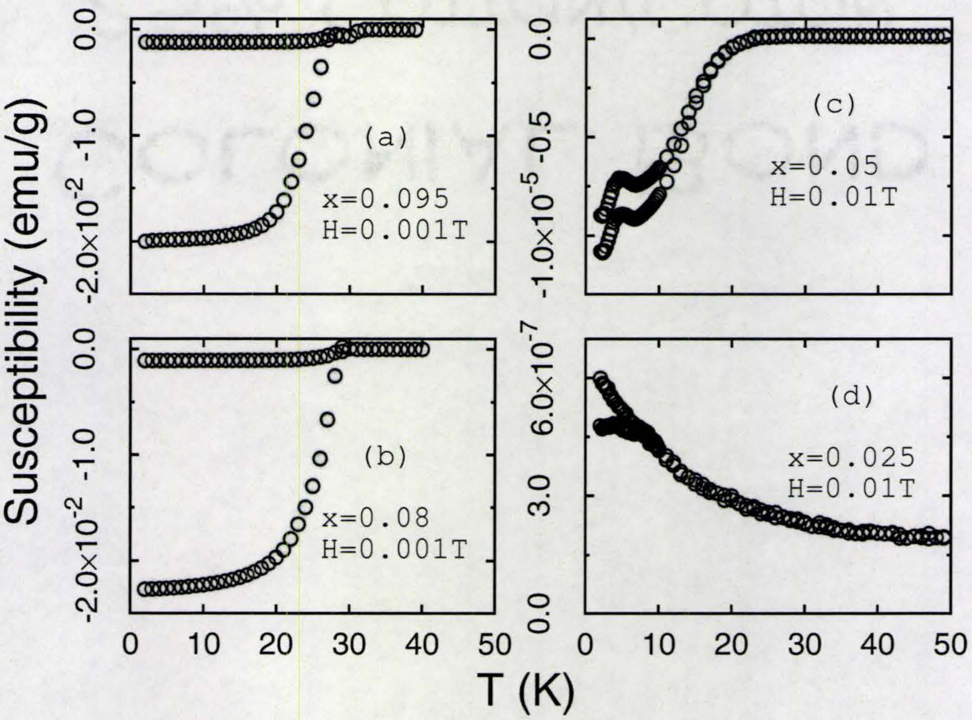

Figure 2.3: SQUID measurements of $La_{2-x}Ba_xCuO_4$ samples with a) x=0.095, b) x=0.08, c) x=0.05 and d) x=0.025.

Figure 2.3 shows the ac susceptibility measurements with four different doping levels using the Superconducting Quantum Interference Device (SQUID) magnetometer. All crystals used for SQUID measurements as shown here are taken from the same growth used for our X-ray and neutron studies. We studied crystals displaying both the spin-glass-like and superconducting regimes of the phase diagram. For single crystals samples with relatively high doping, x=0.095 and 0.08, the SQUID susceptibility measurements show diamagnetic response during zero field cooling protocols (2.3 a and b). The results of the SQUID measurement indicate a bulk superconducting transition at T_c=27 K and 29 K for x=0.095 and 0.08 crystals, respectively. With the lower doping levels x=0.05, a weak superconducting phase transition occurs around 20 K, as evidenced by the weak diamagnetic response which is roughly two orders of magnitude smaller than that displayed by the x=0.08 sample, as shown in figure 2.3 c). Subsequently, history dependent behaviour develops below 10 K in the x=0.05 sample and a peak in the susceptibility is observed at 5 K, indicating a spin-glass ground state. At the lowest Ba concentration, SQUID measurements indicate that the x=0.025 sample also undergoes a spin glass-like transition below ~10 K, as shown in figure 2.3 1d). No signature of long range antiferromagnetic order is observed up to 300 K in the x=0.025 sample, setting a lower limit on the doping level of x>0.02, by comparison with the suppression of the Néel order in $La_{2-x}Sr_xCuO_4$.

All the crystals which are described in this thesis are the best quality single crystals at each doping level. We did several growths for every doping levels, each with identical growth conditions. After the as-grown crystals were surveyed with X-ray and neutrons, only the best quality single crystals at each doping level were selected to perform the comprehensive X-ray and neutron experiments. These experiment results will be discussed in Chapter 4 and 5. The single crystal samples used for the experiments are also extremely stable and give the consistent results from the different measurements regardless of the time or the experiment methods.

Chapter 3

X-ray and neutron scattering techniques

3.1 Introduction

X-ray and neutron scattering techniques are essential experimental tools to study a wide range of phenomena in condensed matter research. Both X-rays and neutrons use their wave-like form to inform on the structure of materials. X-rays interact with electrons in the material. X-ray diffraction typically allows people to study the crystalline structure of materials, although it possible to perform magnetic X-ray diffraction experiments under favourable conditions. While the neutron has no charge but a magnetic moment, and it can interact either with the nucleus through the strong interaction (nuclear scattering) or with unpaired electrons through a magnetic interaction (magnetic scattering). Neutron scattering can also be classified as elastic scattering or inelastic scattering depending on the energy transfer involved. Elastic neutron scattering can be used to determine the crystalline or magnetic structure of materials. Inelastic neutron scattering allows people to measure the elementary excitations in materials, primarily phonons and magnons in crystals. Before we discuss our X-ray and neutron scattering study results on the $La_{2-x}Ba_xCuO_4$ single crystals which we grew, this chapter will discuss the X-ray and neutron scattering techniques themselves. I will also introduce the triple-axis and time-of-flight spectrometers used in our experiments.

3.2 Basic principles of X-ray and neutron scattering

X-ray and neutron scattering follow similar basic concepts in quantum mechanics. Treated as wave-forms, X-ray and neutron wavelengths and their momenta have the following relation.

$$\vec{p} = \hbar\vec{k}, |\vec{k}| = \frac{2\pi}{\lambda} \tag{3.1}$$

where $\vec{k}$ is the associate wave-vector. During the scattering process, the incident wave-vector and energy $\vec{k}$, E, scattered wave-vector and energy $\vec{k}'$, E' as well as the momentum and energy transfer Q, $\triangle$E respectively, must obey momentum and energy conservation (See Fig 3.1).

$$\begin{aligned} \vec{Q} &= \vec{k} - \vec{k}' \\ \triangle E = E - E' &= \begin{cases} \hbar c(k - k') & \text{(X-ray)} \\ \frac{\hbar^2}{2m_n}(k^2 - k'^2) & \text{(neutron)} \end{cases} \end{aligned} \tag{3.2}$$

The energy transfer, $\triangle$E can be zero, positive or negative. Zero energy transfer scattering denotes elastic scattering or diffraction. Non-zero energy transfer scattering denotes inelastic scattering and positive and negative energy transfers depend on whether the X-ray or neutron gives energy to the sample or takes energy from the sample.

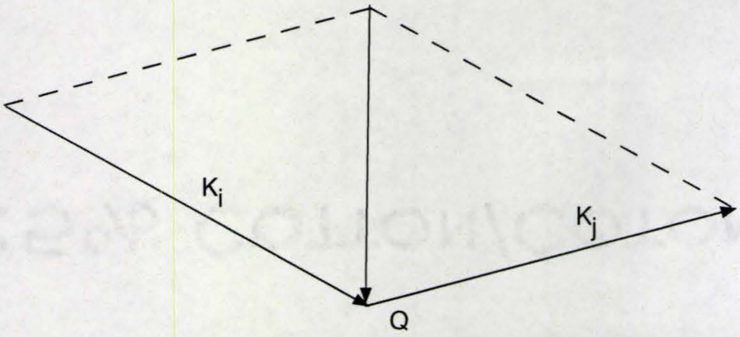

Figure 3.1: Schematic diagram of scattering geometry

In elastic scattering case, $\triangle$E=0, and the X-ray or neutron is scattered from a static crystal. Maximum elastic scattering occurs when there is constructive interference from parallel planes a distance d apart, giving rise to the familiar Bragg's law

$$\lambda = 2d\sin(\theta) \tag{3.3}$$

Comparing X-ray and neutron scattering, X-ray interacts with electrons in the crystal and are used primarily to determine the crystal structure of materials. The neutron has charge zero and a spin 1/2 magnetic moment, and it can interacts with nuclei and magnetic moments in materials. Neutron scattering is used to determine the magnetic ordering and spin excitations in crystals as well as to determine nuclear, or chemical structure. It is particularly important in determining the structure of materials composed of light elements, such as oxides and hydrogenous materials.

3.3 X-ray scattering technique

3.3.1 X-ray scattering formula from crystals

The elastic X-ray scattered intensity formula can be derived following three considerations: 1) The scattering by a single electron, 2) The scattering by an atom, 3) The scattering by a small crystal. A detailed discussion of these can be found in many X-ray scattering books, for example (Zachariasen, 1945).

First consider monochromatic incident X-rays scattered by an electron at the origin with charge $-e$ and mass m. The incident plane wave of X-rays

$$\vec{E}_i = \vec{E}_0 e^{i\omega_0 t - i\vec{k}\cdot\vec{r}} \tag{3.4}$$

act on the electrons. Where $\vec{E}_0$ is the incident electric field vector and $\vec{k}$ is incident wave vector. The electron oscillates due to the electric force it experiences. The oscillating electron radiates an electromagnetic wave with the same frequency, i.e. the scattered X-rays

$$e^{i\omega_0 t}\vec{E}_s = (\vec{u} \times \frac{-e^2}{m\omega_0^2}\vec{E}_0) \times \vec{u}\frac{\omega_0^2}{c^2 R} e^{i\omega_0 t - i\vec{k}\cdot\vec{R}} \tag{3.5}$$

Where $\vec{R} = R\vec{u}$, $\vec{u}$ is the unit vector pointing to scattering direction. The average intensity of scattered radiation is $I = \frac{c}{8\pi}E^2$. Using the above equations, the scattered intensity is

$$I_s = I_0(\frac{e^2 \sin\phi}{mc^2 R})^2 \tag{3.6}$$

where ϕ is the angle between $\vec{E}_0$ and scattering direction $\vec{u}$.

With unpolarized X-rays, we take the average value of $\sin^2\phi$, and equation 3.6 becomes:

$$I_s = I_0(\frac{e^2}{mc^2 R})^2(\frac{1+\cos^2 2\theta}{2}) \tag{3.7}$$

where 2θ is the scattering angle. This is the famous J. J. Thomson scattering formula for X-rays. It shows the scattered intensity to be independent of the incident frequency. Also it shows the intensity to be inversely proportional to the square of the particle mass. That's why the X-ray scattering only considers interactions with electrons, rather than with much heavier nuclei.

Next, we consider X-ray scattering by an atom, which means scattering from a number Z of different electrons which are bounded in a small volume. Each electron can be treated as a free electron and we use the same free electron scattering formula. The total intensity will be the sum from each individual electron. However the scattered wave from electrons at different positions will acquire different phases. This phases difference makes the scattered intensity weaker at finite scattering angle. The total scattered intensity can be written as

$$I_s = I_0(\frac{e^2}{mc^2R})^2(\frac{1+\cos^2 2\theta}{2})f^2 \tag{3.8}$$

where f is called atomic form factor with a general expression

$$f^0(\vec{q}) = \int \rho(\vec{r})e^{i\vec{q}\cdot\vec{r}}dV \tag{3.9}$$

The value of the f decreases as the scattering vector $\vec{q}$ increases. The maximum value of f depend on the electron density within the atoms. Heavy atoms with more electrons will have higher values than light atoms. Because of this property, X-ray scattering is not particularly sensitive to light atoms, especially materials containing H.

Finally, we consider X-ray scattering from a small crystal. Atoms are placed at periodic positions in the lattice. Using a similar discussion to that we described before, the intensity of the scattering close to a maximum, I_Q

may be written as

$$I_Q = I_s|F_Q|^2 \prod_i \frac{\sin^2 \frac{1}{2} N_i \vec{Q} \cdot \vec{a}_i}{\sin^2 \frac{1}{2} \vec{Q} \cdot \vec{a}_i} \tag{3.10}$$

where F_Q is called structure factor

$$F_Q = \sum_n f_n e^{iQ \cdot r_n} \tag{3.11}$$

With large number, N, of unit cells in the volume of a small crystal, the intensity I_Q peaks up at $\frac{1}{2}\vec{Q} \cdot \vec{a}_i = n\pi$. This should be compared with the reciprocal lattice postion $G = \sum n_i 2\pi/a_i$ This means that, when the transfer wave vector transfer $\vec{Q} = \vec{k}_s - \vec{k}_i$ is equal to a reciprocal lattice point $\vec{G}$, the intensity of the scattering reaches a maximum. Replacing the value of $Q = 2\pi \sin\theta/\lambda$ and $G = n2\pi/d$, we get the familiar Bragg's law $2d \sin\theta = n\lambda$.

3.3.2 X-ray sources and the experimental configuration

X-ray sources used for scattering measurements usually are either in-house rotate-anode generators or synchrotron radiation sources. Synchrotron radiation is provided at large-scale accelerator facilities and results in very high intensity X-ray beam. In-house rotating-anode X-ray generators are used at universities and small laboratories. The X-ray scattering measurements on $La_{2-x}Ba_xCuO_4$ single crystals reported in this thesis were carried on a rotating-anode X-ray generator with a Cu target at McMaster University.

The basic constituents of an X-ray generator are an intense source of electrons, a large voltage potential V to accelerate the electrons to high energy, and a target or a anode which rotates. Electrons strike the target and generate a continuous spectrum of radiation due to the rapid deceleration of the electrons. The wavelength of this radiation depends on the energy loss of the electrons, $\triangle E = hv$. Since the energy loss of electrons in these processes are not same, the radiation has a continuous energy spectrum. The lowest wavelength is limited by the maximum acceleration voltage V. So the lower cutoff wavelength, λ_{min} is defined as

$$\begin{aligned} eV = hv_{max} = \frac{hc}{\lambda_{min}} \\ \lambda_{min} = \frac{hc}{eV} \end{aligned} \tag{3.12}$$

When the acceleration voltage exceeds a specific value, which depend on the target materials, a characteristic spectrum to the radiation appears in the form of sharp and intense peaks. This characteristic spectrum originates from the electron transitions between the inner shell electronic states of atoms. Using a classical shell model, we can describe the electronic structure of atoms as a series of shells which are labeled as K, L, M,...corresponding to increasing distance from nucleus. The electronics in the K, L, M shells also correspond to principle quantum numbers n=1, 2, 3,... When an accelerated electron has sufficiently high energy, it can knock an electron out of an inner shell state to a higher energy state. An electron at a higher energy level will fill up the vacancy left behind and X-ray photons with an associated energy corresponding to the energy difference between levels will be emitted. Because the energy of these X-ray photons depends on the energy gap between the appropriate levels, these emitted X-ray photons are monochromatic and characteristic of the materials which make up the target. Nearly all the X-ray scattering studies use the characteristic spectrum of the target as they mostly require a monochromatic incident beam.

The characteristic lines are labeled according to the lower electronic level involved in the transition process. For example, K_α and K_β radiation indicates electron jumps from the L and M shell to the K shell, respectively. The common Cu K radiation used in our lab has following characteristic wavelength.

$$\begin{aligned} K_{\alpha 1} &: 1.54051\mathring{A} \\ K_{\alpha 2} &: 1.54433\mathring{A} \\ K_{\beta 1} &: 1.39217\mathring{A} \end{aligned} \tag{3.13}$$

The doublet of Cu K_α radiation originates from the fine structure of L shells of Cu atoms.

Often in X-ray scattering measurements, the X-ray beam after the target is further selected for a single incident wavelength using a single crystal monochromator, such as pyrolytic graphite crystals or Ge single crystals. In this thesis, we will discuss high-resolution X-ray diffraction measurements. In order to measure the Bragg scattering angle 2θ as precisely as possible, we must separate the $K_{\alpha 1}$ and $K_{\alpha 2}$ components of the incident radiation. We used perfect Ge (111) as our monochromator. Furthermore, we employed 2 series of slits to block the $K_{\alpha 2}$ beam after the monochromator and narrow down the incident beam reducing its angular divergence. With all above carefully adjusted, we produced a 1 mm wide $K_{\alpha 1}$ X-ray beam at the sample, without $K_{\alpha 2}$ contamination.

3.4 Neutron scattering techniques

3.4.1 Properties of neutrons

The neutron has zero charge and an s=1/2 magnetic moment. Unlike X-rays which interact with electrons in crystals, neutrons directly interact with nuclei or the magnetic moments associated with unpaired electrons in magnetic atoms. So neutron scattering has two relevant cross sections: those pertaining to 1) nuclear scattering, and to 2) magnetic scattering. For nuclear scattering, neutrons interact via the strong interaction with nuclei and the scattering depends on the nuleiar isotope of the atom in question. This means that not only can neutron scattering detect the light elements but it also can distinguish between isotopes of the same elements. Magnetic neutron scattering can provide the information on the magnetic ordering and excitations in magnetic materials.

The properties of neutron make it a very desirable tool to probe the structure and dynamics of materials. For typical thermal neutrons, the de Broglie wavelength is of the order of inter-atomic distances in solids and liquids. People use the wavelength, wave-vector, velocity, energy and characteristic temperature to characterize the momentum and energy of neutrons. Their relationship between these are

$$E = k_BT = \frac{1}{2}mv^2 = \frac{h^2}{2m\lambda^2} = \frac{\hbar^2k^2}{2m} \tag{3.14}$$

with the neutron mass and values of the constants h, k_B inserted, these relationships become

$$\begin{aligned} \lambda &= 6.283\frac{1}{k} = 3.956\frac{1}{v} = 9.045\frac{1}{\sqrt{E}} = 30.81\frac{1}{\sqrt{T}} \\ E &= 0.08617T = 5.227v^2 = 81.81\frac{1}{\lambda^2} = 2.072k^2 \end{aligned} \tag{3.15}$$

The quantities in these equations have the following units: λ in Å, k in 10^{10}m^{-1}, v in kms^{-1}, E in meV and T in K. The neutron energy is sometimes expressed in terms of its frequency with THz as unit. The appropriate conversion between meV and THz is 1 THz=4.132 meV.

3.4.2 Nuclear scattering

Neutron scattering results usually are expressed in terms of a $cross-section$. The definition and derivation of the cross-section used in this thesis closely follow the discussion in the book by Squires (Squires, 1978). The *total scattering cross-section* σ_{tot}, *differential cross-section* $d\sigma/d\Omega$ and *partial differential cross-section* $d^2\sigma/(d\Omega dE')$ are defined as

$$\sigma_{tot} = (\text{total number of neutrons scattered per second})/\Phi$$

$$\frac{d\sigma}{d\Omega} = \begin{array}{l}(\text{number of neutrons scattered} \\ \text{per second into solid angle } d\Omega)/\Phi d\Omega\end{array} \tag{3.16}$$

$$\frac{d^2\sigma}{d\Omega dE'} = \begin{array}{l}(\text{number of neutrons scattered per second into} \\ \text{solid angle } d\Omega \text{ with final energy } E' + dE')/\Phi d\Omega dE'\end{array}$$

where Φ is the flux of incident beam and $d\Omega$ is a small solid angle in the scattered neutron direction θ, ϕ. The relations between these definitions are

$$\begin{aligned} \sigma_{tot} &= \int_{\Omega} (\frac{d\sigma}{d\Omega}) d\Omega \\ \frac{d\sigma}{d\Omega} &= \int_{0}^{\infty} (\frac{d^2\sigma}{d\Omega dE'}) dE' \end{aligned} \tag{3.17}$$

Using a similar discussion to that used in discussing the X-ray scattering formula, we first consider scattering from a fixed nucleus. In this simple case, the wavelength of the neutrons is usually much larger than the object causing the scattering. In this case, the scattered wave is a spherically symmetric S wave. The incident wave and scattered wave can be written as

$$\begin{aligned} \psi_{inc} &= e^{i\vec{k}\cdot\vec{z}} \\ \psi_{sc} &= -\frac{b}{r} e^{i\vec{k}\cdot\vec{r}} \end{aligned} \tag{3.18}$$

where b is a constant value with units of length which is called the scattering length and is different for each nucleus. Typical values of b lie in the range of

10^{-15}m. The negative sign used in the equation above is required such that a positive value of b corresponding to a repulsive potential. If the neutrons have a velocity v, the cross-section is

$$\begin{aligned} \frac{d\sigma}{d\Omega} &= \frac{v|\psi_{sc}|^2}{v|\psi_{inc}|^2} = b^2 \\ \sigma_{tot} &= 4\pi b^2 \end{aligned} \tag{3.19}$$

This equation shows that the total scattered intensity is proportional to the square of scattering length b. Since the value of b varies from nucleus to nucleus, it is possible to measure isotope effects using neutron scattering. In contrast to X-rays, the value of b in hydrogen is very large. Neutron scattering has becomes a very important tool to detect H within the structure and dynamics in solids or liquids.

Next we consider the neutron scattering by a general system. The incident neutrons are characterized by a wavelength λ and a wave-vector $\vec{k}$. After scattering, the final state of the neutron changes to λ' and $\vec{k}'$. Using the definition of differential cross-section, we have

$$\left(\frac{d\sigma}{d\Omega}\right)_{\lambda\to\lambda'} = \frac{1}{\Phi d\Omega}\sum_{\vec{k}'} W_{\vec{k},\lambda\to\vec{k}',\lambda'} \tag{3.20}$$

where $W_{\vec{k},\lambda\to\vec{k}',\lambda'}$ is the number of neutrons per second changing from state $\vec{k}.\lambda$ to $\vec{k}'.\lambda'$. Φ is the flux of incident neutrons. By applying Fermi's Golden rule and inserting the density of final state at $\vec{k}'$, we get

$$\left(\frac{d\sigma}{d\Omega}\right)_{\lambda\to\lambda'} = \frac{k'}{k}\left(\frac{m}{2\pi\hbar^2}\right)^2 | < \vec{k}'\lambda'|V|\vec{k}\lambda > |^2 \tag{3.21}$$

Using E and E_λ for the initial energy of the neutrons and the system, and E' and $E_{\lambda'}$ for the final energy of the neutrons and the system and, with energy conservation, we get *partial differential cross-section*

$$\left(\frac{d\sigma}{d\Omega dE'}\right)_{\lambda\to\lambda'} = \frac{k'}{k}\left(\frac{m}{2\pi\hbar^2}\right)^2 | < \vec{k}'\lambda'|V|\vec{k}\lambda > |^2\delta(E_\lambda - E_{\lambda'} + \hbar\omega) \tag{3.22}$$

where $\hbar\omega = E - E'$.

By assuming the potential V is of short range, and comparing this expression with *differential cross-section* expression for fixed atoms in Equ. 3.19. We see V can be written as

$$V(\vec{r}) = \frac{2\pi\hbar^2}{m} b\delta(\vec{r}) \tag{3.23}$$

This potential is known as the Fermi pseudopotential and will be used in later discussion. The positive value of b results from a repulsive potential.

In order to obtain a general form of *partial differential cross-section*, we substitute Equ. 3.23 into Equ 3.22. Then we apply a Fourier transform to the potential and use the integral expression of the delta function in energy. Also, we need to sum over the λ, λ' to get an equation suitable for real experiments. Finally, the *partial differential cross-section* can be written as

$$\frac{d\sigma}{d\Omega dE'} = \frac{k'}{k}\frac{1}{2\pi\hbar}\sum_{jj'} b_j b_{j'} \int_{-\infty}^{\infty} < e^{-i\vec{Q}\cdot\vec{R}_{j'}(0)} e^{i\vec{Q}\cdot\vec{R}_j(t)} > e^{-i\omega t} dt \tag{3.24}$$

where $\vec{Q} = \vec{k} - \vec{k'}$ is scattering vector. $\vec{R}$ is position of the nucleus in material.

Now imagine that we have a scattering system with a large number of nuclei of just a single element. The scattering length b varies from one nucleus to another due to isotopes or nuclear spin states. The measured cross-section is very close to the average value using $\bar{b}$ instead. Assuming no correlations between b value at different nuclei

$$\begin{aligned} \overline{b_j, b_{j'}} &= (\bar{b})^2, \quad j \neq j' \\ \overline{b_j, b_{j'}} &= \bar{b^2}, \quad j = j' \end{aligned} \tag{3.25}$$

Equ 3.24 changes to

$$\frac{d\sigma}{d\Omega dE'} = \frac{k'}{k}\frac{1}{2\pi\hbar}(\bar{b})^2\sum_{jj'}\int_{-\infty}^{\infty} < e^{-i\vec{Q}\cdot\vec{R}_{j'}(0)}e^{i\vec{Q}\cdot\vec{R}_j(t)} > e^{-i\omega t}dt$$
$$+ \frac{k'}{k}\frac{1}{2\pi\hbar}[\bar{b^2} - (\bar{b})^2]\sum_{j}\int_{-\infty}^{\infty} < e^{-i\vec{Q}\cdot\vec{R}_{j}(0)}e^{i\vec{Q}\cdot\vec{R}_j(t)} > e^{-i\omega t}dt \quad (3.26)$$

The first term in the above equation is the *coherent cross-section* while the second term is the *incoherent cross-section.* Then we can separate the two terms into

$$\begin{aligned}\left(\frac{d\sigma}{d\Omega dE'}\right)_{coh} &= \frac{\sigma_{coh}}{4\pi}\frac{k'}{k}\frac{1}{2\pi\hbar}\sum_{jj'}\int_{-\infty}^{\infty} < e^{-i\vec{Q}\cdot\vec{R}_{j'}(0)}e^{i\vec{Q}\cdot\vec{R}_j(t)} > e^{-i\omega t}dt \\ \left(\frac{d\sigma}{d\Omega dE'}\right)_{inc} &= \frac{\sigma_{inc}}{4\pi}\frac{k'}{k}\frac{1}{2\pi\hbar}\sum_{j}\int_{-\infty}^{\infty} < e^{-i\vec{Q}\cdot\vec{R}_{j}(0)}e^{i\vec{Q}\cdot\vec{R}_j(t)} > e^{-i\omega t}dt\end{aligned} \quad (3.27)$$

where

$$\sigma_{coh} = 4\pi(\bar{b})^2, \quad \sigma_{inc} = 4\pi[\bar{b^2} - (\bar{b})^2] \quad (3.28)$$

Equ 3.27 shows that the coherent scattering includes correlations from all nuclei. It gives the information as to interference effects in the system. However, the incoherent scattering depends only on the correlations from same nucleus at different times. As such, it does not give any interference information.

If we write Equ. 3.27 in the form

$$\begin{aligned}\left(\frac{d\sigma}{d\Omega dE'}\right)_{coh} &= \frac{\sigma_{coh}}{4\pi}\frac{k'}{k}NS(\vec{Q},\omega) \\ \left(\frac{d\sigma}{d\Omega dE'}\right)_{inc} &= \frac{\sigma_{inc}}{4\pi}\frac{k'}{k}NS_i(\vec{Q},\omega)\end{aligned} \quad (3.29)$$

where

$$\begin{aligned}S(\vec{Q},\omega) &= \frac{1}{N}\frac{1}{2\pi\hbar}\sum_{jj'}\int_{-\infty}^{\infty} < e^{-i\vec{Q}\cdot\vec{R}_{j'}(0)}e^{i\vec{Q}\cdot\vec{R}_j(t)} > e^{-i\omega t}dt \\ S_i(\vec{Q},\omega) &= \frac{1}{N}\frac{1}{2\pi\hbar}\sum_{j}\int_{-\infty}^{\infty} < e^{-i\vec{Q}\cdot\vec{R}_{j}(0)}e^{i\vec{Q}\cdot\vec{R}_j(t)} > e^{-i\omega t}dt\end{aligned} \quad (3.30)$$

$S(\vec{Q},\omega)$ and $S_i(\vec{Q},\omega)$ are known as the scattering functions and are closely related to the coherent and incoherent cross-section. $S(\vec{Q},\omega)$ is also called the dynamic structure factor. These expressions are only determined by the properties of the materials and are not by the properties of neutrons or the scattering process.

Finally, we consider scattering from a single crystal with a Bravais lattice. The instantaneous positions of the nuclei j can be written as

$$\vec{R}_j = \vec{l} + \vec{u}_j \tag{3.31}$$

where $\vec{u}_j$ is the displacement of the nucleus from its equilibrium position $\vec{l}$. So the correlations in a Bravais lattice crystal only depends on $\vec{l}-\vec{l}'$. Also within the harmonic approximation of the crystal, the coherent scattering function in Equ. 3.30 is

$$S(\vec{Q},\omega) = \frac{1}{2\pi\hbar} e^{-2W} \sum_j e^{i\vec{Q}\cdot\vec{l}} \int_{-\infty}^{\infty} e^{<[\vec{Q}\cdot\vec{u}_0(0)][\vec{Q}\cdot\vec{u}_j(t)]>} e^{-i\omega t} dt \tag{3.32}$$

where

$$2W = < [\vec{Q}\cdot\vec{u}_0(0)]^2 > \tag{3.33}$$

e^{-2W} is known as the Debye-Waller factor. It is the term in Equ. 3.32 which contains the effects due to thermal vibration of the nuclei. Since $< [\vec{u}_0(0)]^2 >$ increases with temperature, the Bragg scattering intensity decreases but is not eliminated.

If we expand the term $e^{<[\vec{Q}\cdot\vec{u}_0(0)][\vec{Q}\cdot\vec{u}_j(t)]>}$ in

$$e^{<[\vec{Q}\cdot\vec{u}_0(0)][\vec{Q}\cdot\vec{u}_j(t)]>} = \sum_m \frac{1}{m!} \left(< [\vec{Q}\cdot\vec{u}_0(0)][\vec{Q}\cdot\vec{u}_j(t)] > \right)^m \tag{3.34}$$

the mth term gives the contribution to the scattering from m-phonon process. The first two terms, m=0 and m=1, gives the elastic and the one phonon scattering functions. For elastic scattering, m=0, and this term equals the constant value 1. This gives the Bragg's law as we discussed in the X-ray scattering section. For one phonon scattering, m=1, the term gives $<[\vec{Q}\cdot\vec{u}_0(0)][\vec{Q}\cdot\vec{u}_j(t)]>$ and will produce thermal factors $<n_s(\vec{Q})>$ and $1+<n_s(\vec{Q})>$,

$$<n_s(\vec{Q})>=\frac{1}{e^{\hbar\omega_{\vec{Q}}\beta}-1} \tag{3.35}$$

corresponding to phonons being absorbed or emitted, respectively. These factors are also known as Bose factors for the process of creating or absorbing Bose-Einstein particles.

3.4.3 Magnetic scattering

Neutrons are not only scattered by nuclei but also by magnetic moments in solids. The magnetic dipole moment operator of the neutron is

$$\vec{\mu}_n=-\gamma\mu_N\vec{\sigma}, \quad \mu_N=\frac{e\hbar}{2m_p} \tag{3.36}$$

γ is a positive constant value equal 1.913. μ_N is the nuclear magneton. m_p is proton mass. σ is the Pauli spin operator with eigenvalues ±1.

The magnetic dipole moment operator of an electron is

$$\vec{\mu}_e=-2\mu_B\vec{s}, \quad \mu_e=\frac{e\hbar}{2m_e} \tag{3.37}$$

μ_B is the Bohr magneton. m_e is the mass of electron. $\vec{s}$ is the spin angular momentum operator with eigenvalues $\pm\frac{1}{2}$.

The magnetic interaction between neutrons and unpaired electrons comes from both spin and orbital components of the electronic magnetic moment. The magnetic interaction potential can be written as

$$V_m=-\vec{\mu_N}\cdot\vec{B}=-\frac{\mu_0}{4\pi}\gamma\mu_N 2\mu_B\vec{\sigma}\cdot\left[\nabla\times\left(\frac{\vec{s}\times\vec{R}}{|R|^3}\right)+\frac{1}{\hbar}\frac{\vec{p}\times\vec{R}}{|R|^3}\right] \tag{3.38}$$

The first term in the square bracket is the spin contribution while the second is the orbital contribution.

Similar to the Equ. 3.22 we used for nuclear scattering, the magnetic scattering partial differential cross-section is written in the form

$$\left(\frac{d\sigma}{d\Omega dE'}\right)_{\sigma\lambda\to\sigma'\lambda'} = \frac{k'}{k}\left(\frac{m}{2\pi\hbar^2}\right)^2 | < \vec{k}'\vec{\sigma}'\lambda'|V_m|\vec{k}\vec{\sigma}\lambda > |^2\delta(E_\lambda - E_{\lambda'} + \hbar\omega) \tag{3.39}$$

This is the cross-section for neutrons scattered by the magnetic interaction with all electrons. The incident and scattered neutrons are described by the state $\vec{k}, \vec{\sigma}, \lambda$ and $\vec{k}', \vec{\sigma}', \lambda'$, respectively.

Substituting the magnetic potential V_m 3.38 into 3.39 and performing the summation gives the result

$$\left(\frac{d\sigma}{d\Omega dE'}\right)_{\sigma\lambda\to\sigma'\lambda'} = (\gamma r_0)^2\frac{k'}{k}| < \vec{\sigma}'\lambda'|\vec{\sigma}\cdot\vec{D}_\perp|\vec{\sigma}\lambda > |^2\delta(E_\lambda - E_{\lambda'} + \hbar\omega) \tag{3.40}$$

where

$$\begin{gathered} \vec{D}_\perp = \sum_i e^{i\vec{Q}\cdot\vec{r}_i}\left[\hat{Q}\times(\vec{s}_i\times\hat{Q} + \frac{i}{\hbar Q}(\vec{p}_i\times\hat{Q}\right] \\ r_0 = \frac{\mu_0}{4\pi}\frac{e^2}{m_e} \end{gathered} \tag{3.41}$$

The operator $\vec{D}_\perp$ is related to the magnetization of the scattering system. $\hat{Q}$ is the unit vector in the direction of scattering vector $\vec{Q}$. r_0 is the classical electron radius with value 2.818×10^{-15}m. Comparing Equ. 3.41 with that corresponding to nuclear scattering, we see that r_0 and b are of the same order of magnitude. Therefore, the scattering intensities due to nuclear and magnetic scattering are comparable. In addition, the geometry of $\vec{D}_\perp$ shows that it is always perpendicular to the scattering vector $\vec{Q}$. This means that only the component of magnetic moment perpendicular to $\vec{Q}$ scan can be detected by the neutron. This feature of magnetic neutron scattering make it possible to determine the magnetization direction in the magnetic crystals under favourable conditions.

Similar to the nuclear scattering function, we can use the magnetic scattering function to describe the cross-section.

$$\frac{d\sigma}{d\Omega dE'} = (\gamma r_0)^2 \frac{k'}{k} N[\frac{1}{2} g F(\vec{Q})]^2 S(\vec{Q}, \omega) \tag{3.42}$$

where

$$\begin{aligned} S(\vec{Q}, \omega) = \frac{1}{2\pi\hbar} e^{-2W} \sum_{\alpha\beta} (\delta_{\alpha\beta} - \hat{Q}_\alpha \hat{Q}_\beta) \sum_j e^{i\vec{Q}\cdot\vec{l}} \\ \times \int_{-\infty}^{\infty} e^{<[\vec{Q}\cdot\vec{u}_0(0)][\vec{Q}\cdot\vec{u}_j(t)]>} < S_0^\alpha(0) S_j^\beta(t) > e^{-i\omega t} dt \end{aligned} \tag{3.43}$$

is magnetic scattering function. Like nuclear scattering function, $S(\vec{Q}, \omega)$ is entirely determined by the magnetic properties of materials without the reference to either the incident or scattered neutrons. g is Landé splitting factor. $F(\vec{Q})$ is magnetic form factor. It is related to the unpaired electron density in atoms. Compared to the form factor $f(\vec{Q})$ in X-ray scattering, the magnetic form factor also falls rapidly as increase scattering vector $\vec{Q}$.

For elastic magnetic neutron scattering, the calculation takes the limits of $t \rightarrow \infty$. $< S_0^\alpha(0) S_j^\beta(t) >$ becomes independent of time as $< S_0^\alpha(0) >< S_j^\beta(t) >$. The elastic magnetic scattering function changes to

$$S(\vec{Q}, \omega = 0) = e^{-2W} \sum_{\alpha\beta} (\delta_{\alpha\beta} - \hat{Q}_\alpha \hat{Q}_\beta) \sum_j e^{i\vec{Q}\cdot\vec{l}} < S_0^\alpha(0) >< S_j^\beta(t) > \tag{3.44}$$

This means that the intensity of elastic magnetic scattering is generally proportional to the square of the staggered magnetic moments $< S^\perp >^2$.

For inelastic magnetic neutron scattering, $S(\vec{Q}, \omega)$ is related to the imaginary part of the dynamic spin susceptibility, $\chi''(\vec{Q}, \omega)$, through the fluctuation dissipation theorem.

$$S(\vec{Q},\omega) = \frac{\chi''(\vec{Q},\omega)}{1 - e^{\hbar\omega/k_B T}} \tag{3.45}$$

Integrating over all wavevectors gives the local susceptibility, $\chi''(\omega)$.

3.4.4 Triple-axis and time-of-flight spectrometers

Triple-axis and time-of-flight spectrometer are two types of neutron spectrometers which are used to measure the scattering function $S(\vec{Q},\omega)$. They both can be used for elastic and inelastic neutron scattering studies to meet different experimental requirements. The triple-axis spectrometer is typically used at continuous reactor-based neutron sources. In contrast, time-of-flight spectrometers measure the scattering of neutrons with pulsed incident neutrons. The time-of-flight spectrometer can be placed at a continuous neutron source using mechanical choppers to pulse the incident beam with an ensuring cost in flux.

Triple-axis spectrometers are comprised of a monochromator, a sample rotation stage, an analyzer, detectors and collimators. Figure 3.2a) shows the layout of a triple-axis spectrometer. The three axes are located at the monochromator, the sample and the scattered beam monochromator or analyer. Monochromators and analyzers are usually single crystals or pyrolytic graphite. Neutrons from the reactor have a Maxwellian distribution spectrum of energy. The incident and scattered wavelength, λ, λ', are selected by Bragg's scattering at the monochromator and analyzer. The corresponding scattering angles are $2\theta_M$ and $2\theta_A$ for the monochromator and analyer, respectively. The wavelength, the magnitude of the wave-vector and the energy of the neutrons are related as shown in Equ. 3.15. The direction of the incident and scattered

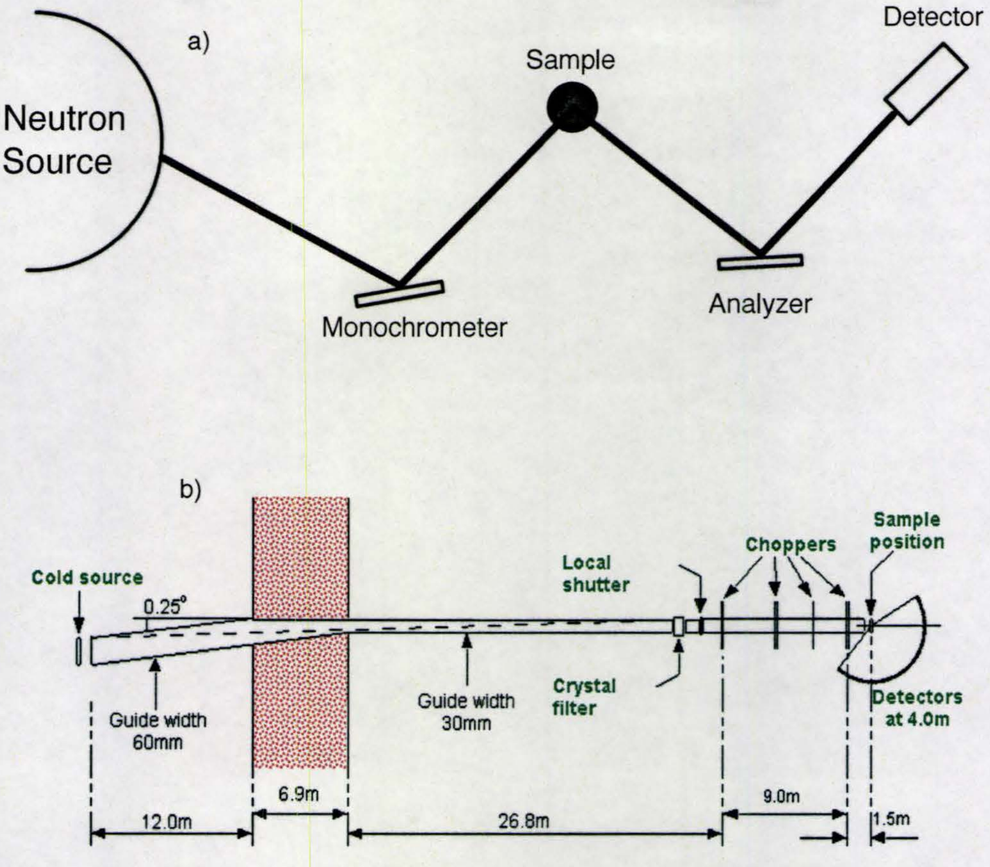

Figure 3.2: Schematic diagram of a triple axis a) and a direct geometry time-of flight spectrometer, such as DCS b)

wave-vector, $\vec{k}, \vec{k}'$, are determined by the geometry of the beam direction before and after the samples. Thus, $\vec{k}, \vec{k}'$ can be easily controlled by the triple-axis spectrometer. By simply applying the relation shown in Equ 3.2, the wave-vector transfer $\vec{Q}$ and energy transfer $\hbar\omega$ can be selected to perform the desired measurements.

One advantage of the triple-axis spectrometer is its flexibility. Usually the measurements are performed in constant E or constant $\vec{Q}$ modes. For constant E mode measurements, scans are performed with the energy transfer fixed and the $\vec{Q}$ of the scattering is scanned. In contrast, constant $\vec{Q}$ mode measurements scans in $\hbar\omega$ space with a fixed momentum transfer $\vec{Q}$. The neutron scattering experiment generally collects data within a four dimensional parameter space $(\vec{Q}, \hbar\omega)$.

One disadvantage of the triple-axis spectrometer is that higher order contamination of neutrons occurs during Bragg scattering at both the monochromator and analyzer crystals. In Bragg's law, neutrons with wavelength λ/n with n=1, 2, 3... all meet the scattering condition and can be collected at detectors. For example, in elastic scattering, neutron scattering data collect at a particular $\vec{Q}$ point are contaminated by data which come from $n\vec{Q}$ with n=2,3... In order to reduce the neutrons with higher order scattering wavelengths, pyrolytic graphite filters or Beryllium filters are usually used for thermal or cold neutron scattering experiments, respectively.

In addition, real crystals are not perfect. Both the monochromator and the analyzer crystals as well as sample itself have mosaic. Mosaic spreads mean the Bragg scattering occurs over a finite range of scattering angles. Collimators are placed along the neutron path to reduce the divergence of the beam. The resolution function, $R(\vec{Q}, \omega)$, of the triple-axis spectrometer is determined by the configuration of the spectrometer and how it is setup (Cooper and Nathans, 1967).

During neutron scattering experiments, the intensity measured is the convolution of the scattering function with the resolution function (Rogge, 1994)

$$I(\vec{Q},\omega) \propto \int S(\vec{Q}-\vec{Q}',\omega-\omega')R(\vec{Q}',\omega)d\omega' d\vec{Q}' \qquad (3.46)$$

We performed our triple-axis neutron scattering on $La_{2-x}Ba_xCuO_4$ single crystals at Chalk River Laboratory with the C5 and the N5 spectrometer, and also at LLB in France with the 4F1 spectrometer. C5 and N5 are typical triple-axis spectrometers, while 4F1 at LLB uses a double monochromator with parallel crystals to reduce the space required by the spectrometer. At Chalk River, we used thermal neutrons to study superconducting $La_{2-x}Ba_xCuO_4$ single crystal samples with x=0.095 and 0.08. The thermal neutron scattering study of the $La_{2-x}Ba_xCuO_4$ x=0.05 single crystal sample at Chalk River was less successful due to relatively poor resolution. With improved resolution on the cold neutron source at LLB, the neutron scattering results for x=0.05 sample were much improved. Table 3.1 is the summary of experiment setups for triple-axis measurements on the $La_{2-x}Ba_xCuO_4$ single crystals. For all experiments, we use pyrolytic graphite(002) as our monochromator and analyzer crystals.

Time-of-flight spectrometers use the time at which a neutron arrives at the detector and its speed to determine the neutron energy. Such measurements can be performed in either direct geometry or inverse geometry. For a direct geometry layout, incident neutrons have a fixed energy and scattered neutrons are recorded by detectors with different energies and scattered angles. In contrast, for an inverse geometry layout, incident neutrons are a "white

Table 3.1: Summary of experiment setups for triple-axis measurements on the single crystals of $La_{2-x}Ba_xCuO_4$

Doping	Instrument	collimation (°)	E_f (meV)	comments
x=0.095	C5 at Chalk River	open-0.8-0.85-1.2	14.7	elastic
x=0.095	C5 at Chalk River	0.54-0.48-0.54-1.2	14.7	$\hbar\omega$=2.07 meV
x=0.095	C5 at Chalk River	0.54-0.79-0.85-2.4	14.7	$\hbar\omega$=3.1 meV
x=0.095	N5 at Chalk River	open-1.5-3.6-open	14.7	(HHL)
x=0.08	C5 at Chalk River	open-0.8-0.85-1.2	14.7	elastic
x=0.05	4F1 at LLB	open-1-1-open	5	cold source

beam" with a recorded time scale, while scattered neutrons are measured with a single energy. An advantage of time-of-flight spectrometers is the capability to measure both the elastic and the inelastic signal at same time. Also time-of-flight spectrometers completely avoid the higher order contaminations problems as they need not use Bragg's law to determine energy.

Figure 3.2b) shows the layout of Disk Chopper Spectrometer (DCS) at NIST center for neutron scattering. DCS use direct geometry from a cold neutron source at the NIST research reactor. Monochromatic incident neutrons are selected by a series of choppers. The momentum and energy transfer, $\vec{Q}, \hbar\omega$, after scattering by the samples are determined by their arrival time at the instrument's 913 detectors located at scattering angles from -30 to 140°.

We used DCS measure the lightly doped $La_{2-x}Ba_xCuO_4$ single crystals. This thesis focused on three doping levels, x=0.08, 0.05 and 0.025 for which we obtained results with DCS. The summary of DCS configuration we employed is listed in Table 3.2. Where λ_{inc} is the incident neutrons wavelength. $\triangle$E is energy resolution.

Table 3.2: Summary of experiment setups for DCS measurements on the single crystals of $La_{2-x}Ba_xCuO_4$

Doping	λ_{inc} (Å)	$\triangle$E (μeV)
x=0.08	4.8	118
x=0.05	4.8	118
x=0.025	6.2	58

Comparing the triple-axis and the time-of-flight spectrometers such as DCS, a DCS-type spectrometer can easily explore a large range of Q space and this feature can be very important in searches for incommensurate Bragg peaks as occurs in underdoped cuperates, like $La_{2-x}Ba_xCuO_4$ single crystals which are studied in this thesis. However, the detectors of DCS spectrometer are installed at the detector bank with fixed angles. The angular resolution of DCS is relatively low and inflexible compared to the triple-axis spectrometer operated with typical collimation.

Chapter 4

X-ray scattering studies of structural phase transitions in underdoped $La_{2-x}Ba_xCuO_4$

4.1 Introduction

This chapter mainly discusses the high resolution X-ray scattering studies of structural phase transitions in relatively highly doped $La_{2-x}Ba_xCuO_4$ single crystals with x=0.125, 0.095 and 0.08. Power law behaviour in the orthorhombic strain, 2(a-b)/(a+b), is observed over a remarkably wide temperature range of the MTO regime in the phase diagram. We find critical exponents associated with HTT to MTO phase transition in all three samples which are consistent with three dimensional XY universality. We compare the complex temperature-composition phase diagram for the location of structural and superconducting phase transitions in underdoped $La_{2-x}Ba_xCuO_4$ single crystals and find good agreement with results on polycrystalline samples previously studied by other groups (Suzuki and Fujita, 1989a,b). The last section of this chapter briefly discusses the orthorhombic strain as a function of doping levels. At low doping levels, x < 0.05, the high value of T_{d1} and the absence of T_{d2} make the determination of doping levels much more difficult. Using the calculated orthorhombic strains at low temperature, we can estimate the doping levels of the relatively lightly doped samples.

4.2 High resolution X-ray scattering measurements

Single crystal samples with approximate dimensions 8 mm×8 mm×1 mm for x=0.125, and 5 mm×5 mm×1 mm for x=0.095 and 0.08, were cut from large single crystals of $La_{2-x}Ba_xCuO_4$. These were sequentially attached to the cold finger of a closed cycle refrigerator and mounted within a four circle x-ray diffractometer in reflection geometry. Cu $K_{\alpha1}$ (λ=1.54041Å) radiation from an 18kW rotating anode x-ray generator was selected using a perfect germanium (111) single crystal monochromator. The energy of x-ray beam was about 8.047 KeV with a penetration depth around 5 μm in $La_{2-x}Ba_xCuO_4$ single crystals . A Bruker Hi-Star multi-wire area detector was placed on the detector arm, 76 cm from the sample allowing an angular resolution of approximately 0.01 degrees to be achieved. All measurements focused on the $(3, 3, 0)_{HTT}$ Bragg peak of the samples, using notation appropriate to the high temperature tetragonal phase. As we were interested in critical phenomena, the sample was mounted in a Be can and in the presence of a helium exchange gas and the sample temperature was stabilized to $\sim$ 0.005 K for all measurements.

4.3 Identification and nature of phases

Two dimensional maps of the scattering around the $(3, 3, 0)_{HTT}$ Bragg peaks of all three x=0.125, 0.095 and 0.08 $La_{2-x}Ba_xCuO_4$ samples were acquired as a function of temperature. Figure 4.1 shows four representative scans at different temperatures for the $La_{2-x}Ba_xCuO_4$ x=0.125 sample located in three different phases. Each data set consisted of a sample angle rock through the Bragg peak which was integrated out of the horizontal Bragg diffraction plane and plotted as a function of scattering angle, 2θ and rocking angle Ω. Figure 4.1 a) and b) are collected just above and below the HTT to MTO phase transition. Figure 4.1 c) shows that the samle is fully in the MTO phase. The fact of two Bragg features can be seen within the MTO phase is indicative of twinning of the crystal in orthorhombic phase. However by directly examining figure 4.1 a) and b), we cannot precisely estimate the phase transition temperature. A longitudinal cut through this two dimensional data set was performed, giving rise to the longitudinal scans shown in figure 4.2 b) for the x=0.125 sample, and figure 4.3 b) for the x=0.095 sample. Similar data sets taken over a more restricted temperature regime for the x=0.08 sample are of similar quality, but are not shown.

These data sets can be put together to display the full temperature dependence of the longitudinal scans, and this is what is shown in figure 4.2 a) and figure 4.3 a) for the x=0.125 and x=0.095 samples, respectively. These data sets clearly show the bifurcation of a single Bragg peak into two, and then back into one, as the temperature is decreased from room temperature to 20 K, signifying the sequence of phase transitions HTT→MTO→LTT. As previously described, the fact of two Bragg features can be seen in a single

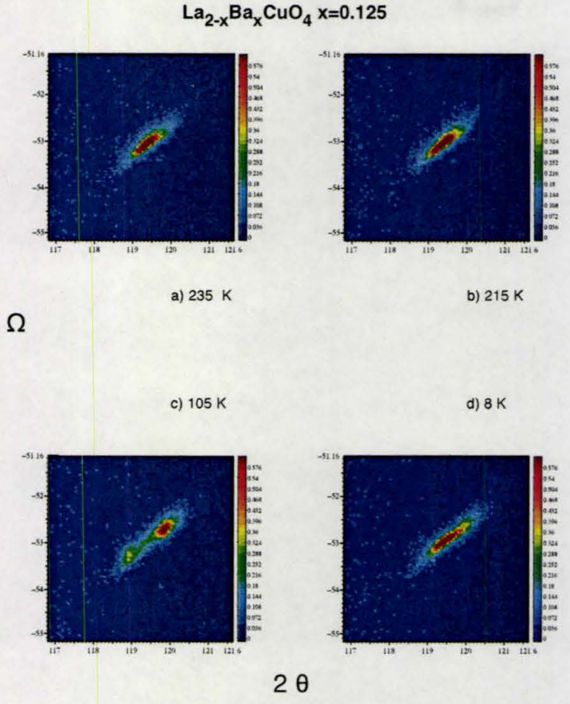

Figure 4.1: High resolution 2 dimensional X-ray diffraction map of (3, 3, 0) of $La_{2-x}Ba_xCuO_4$, x=0.0125 at different temperatures. a) 235 and b) 215 K are just above and below HTT to MTO phase transition, c) 105 K is in MTO phase and d) 8 K is in LTT phase.

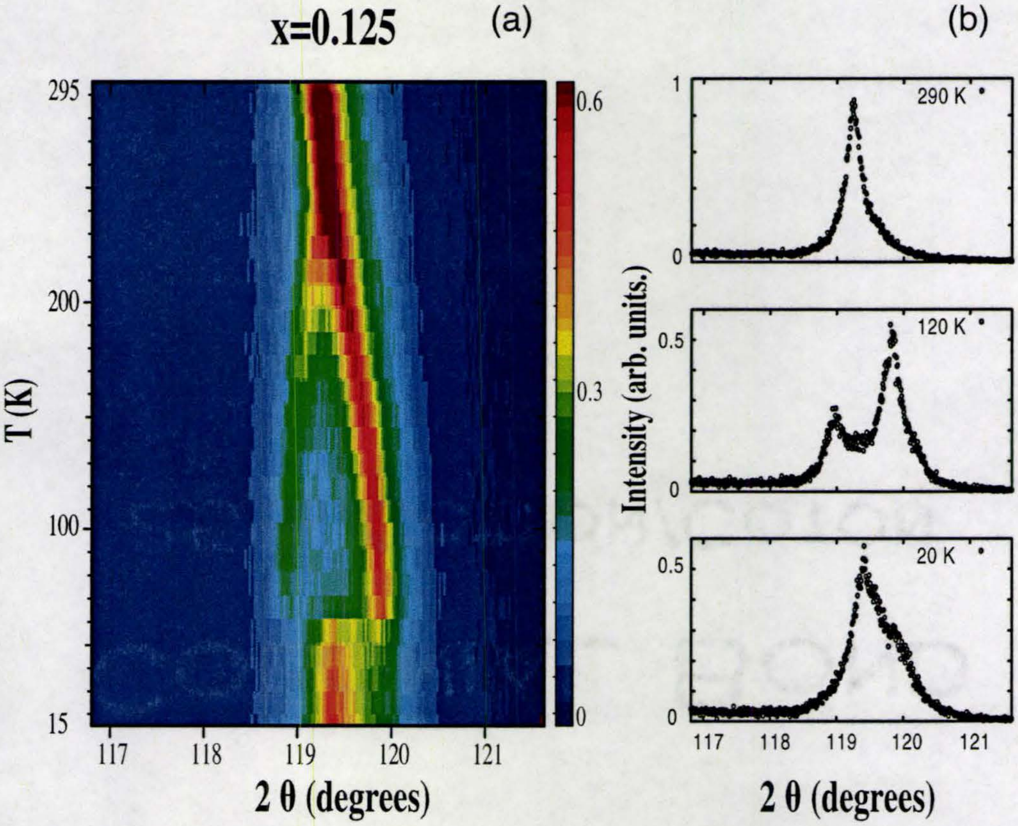

Figure 4.2: (a), High resolution longitudinal scans of the (3, 3, $0)_{HTT}$ Bragg peak in single crystal $La_{2-x}Ba_xCuO_4$, x=0.125 are shown as a function of temperature. (b) Representative longitudinal scans at T=290 K, 120 K, and 20 K from which the color contour map in (a) was made.

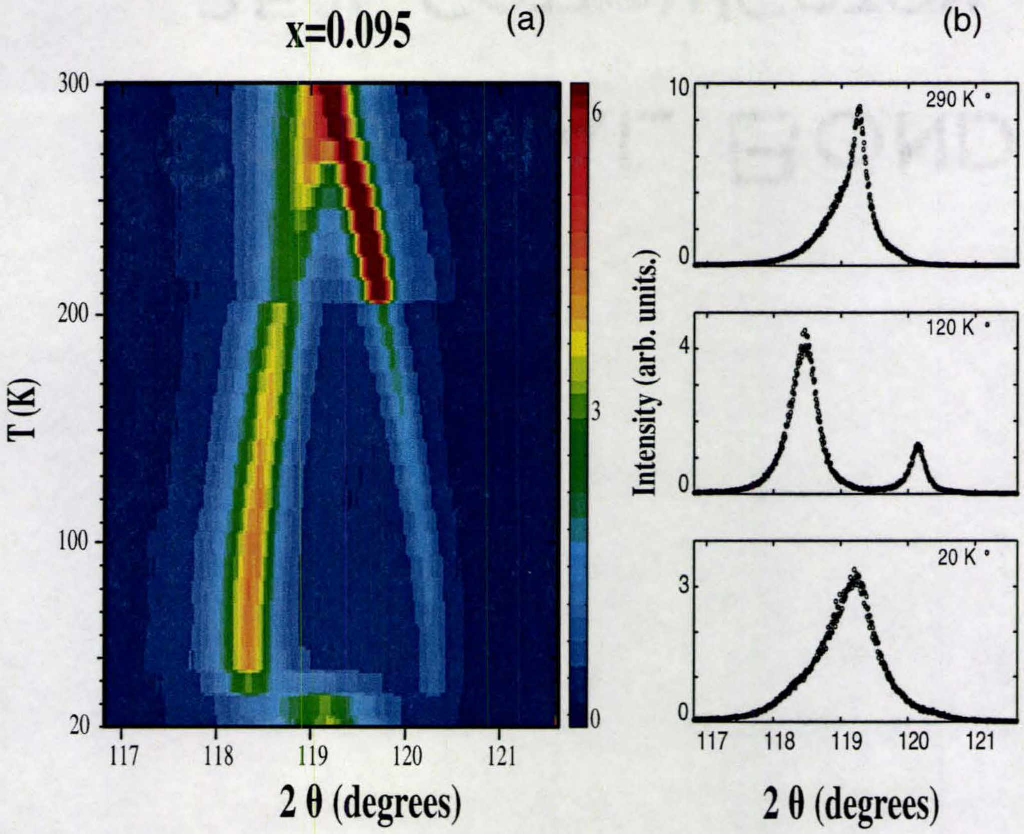

Figure 4.3: (a), High resolution longitudinal scans of the (3, 3, 0)$_{HTT}$ Bragg peak in single crystal $La_{2-x}Ba_xCuO_4$, x=0.095 are shown as a function of temperature. (b) Representative longitudinal scans at T=290 K, 120 K, and 20 K from which the color contour map in (a) was made.

longitudinal scan within the MTO phase is indicative of twinning within the orthorhombic phase, although the two twin domains which are observed do not possess equal volume fractions within the crystal; one Bragg feature is considerably stronger in intensity than the other. A minority and majority twin domain is clearly present, but the relevant volume fraction can change from one thermal cycle to the next. For example, the x=0.095 data set shown in figure 4.3 a) shows data from two independent thermal cycles, one ending with a lowest temperature of ~ 200 K, while the next beginning a new thermal cycle at 200 K. In the first of these, the high angle Bragg peak is the majority domain, while in the second cycle, the lower angle Bragg peak is the majority domain.

The fact that we observe both twin domains in the MTO phase means that the peak positions, the lattice parameters, and consequently the orthorhombic strain, 2(a-b)/(a+b), can be determined as a function of temperature by using Bragg's law. Longitudinal scans of the form shown in figure 4.2b and 4.3b were fit for the purpose of extracting the peak positions in 2θ and therefore the d spacings are associated with the MTO phase.

$$\begin{gathered}\lambda = 2d\sin\theta \\ \Delta(T) = 2\frac{a-b}{a+b} = 2\frac{\sin\theta_b(T) - \sin\theta_a(T)}{\sin\theta_b(T) + \sin\theta_a(T)}\end{gathered} \tag{4.1}$$

This is straightforward for data far removed from the HTT to MTO phase transition, as the two peaks are well defined and separated, as can be seen in the middle panels of figure 4.2b and 4.3b. Closer to the phase transition, one peak may appear as a shoulder to the other, and it is more difficult to ascribe unique values to the two lattice parameters (See Fig4.1 b). We fit these data in two different ways in order to attain robust values for the lattice parameters close to the transition. One of these was to simply fit the longitudinal scans to sums of Lorentzians or Lorentzians raised to an adjustable exponent, while a second technique was to look for zeros in the derivatives of the intensity as a function of 2θ. These gave consistent results for the lattice parameters, giving us confidence that the orthorhombic strain could be estimated accurately close to the transition. However, this technique also gives non-zero values for the orthorhombic strain, albeit relatively small ones, within the HTT phase.

The result of this analysis is shown for all three samples in figure 4.4a. The single $(3, 3, 0)_{HTT}$ Bragg peak breaks into $(6, 0, 0)_{MTO}$ and $(0, 6, 0)_{MTO}$ near T_{d1}=232 K, 272 K and 305 K in the x=0.125, 0.095, and 0.08 samples, respectively, before reforming into a single $(3, 3, 0)_{LTT}$ Bragg peak near T_{d2}=60 K, 45 K, and 35 K, respectively.

Examination of figures 4.2-4.4 shows two qualitative features of the evolving structures. Note that for ease of comparison, the 2θ range of the scattering in figures 4.2 and 4.3 are the same. First, the orthorhomic strain decreases quite substantially with increasing Ba concentration. The lowest temperature strain, for example, in the x=0.125 sample is roughly half that of the x=0.095 sample. Secondly and more importantly, the longitudinal profile of the $(3, 3, 0)_{LTT}$ peak at the lowest temperatures measured, well within the LTT phase, is considerably broader than the corresponding profile of $(3, 3, 0)_{HTT}$. This is true for both the x=0.125 sample and the x=0.095 sample as can be seen by comparing the top and bottom panels of figure 4.2b (for x=0.125) and figure 4.3b (for x=0.095). This shows that the LTT phase is either an admixture of a tetragonal and an orthorhombic phase, as was suggested by electron microscopy on an earlier generation of $La_{2-x}Ba_xCuO_4$ crystals (Zhu et al., 1994), or that it is itself othorhombic with a very small orthorhombic

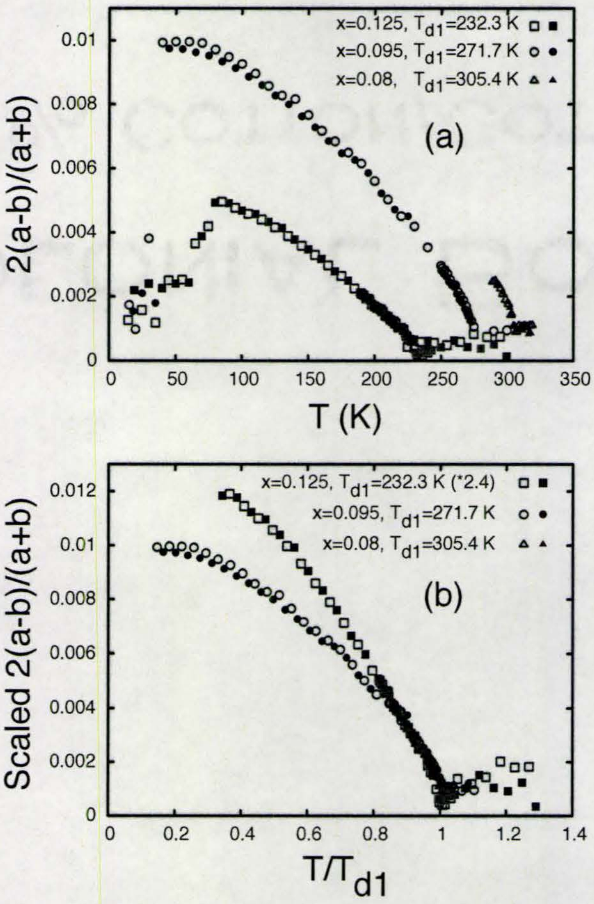

Figure 4.4: (a) The orthorhombic strain vs. temperature is plotted for $La_{2-x}Ba_xCuO_4$ x=0.125, 0.095 and 0.08 single crystal samples. The open and filled symbols represent warming and cooling cycles, respectively. The orthorhombic strain is obtained by fitting longitudinal scans, shown in figures. 4.2 and 4.3. (b) The same orthorhombic strain vs. temperature as in (a) but now plotted vs T/T_{d1} and the strain has been scaled (for the x=0.125 sample, by a factor of 2.4) to emphasize universal behavior for T/T_{d1} greater than 0.8.

strain. In either case it is not as "tetragonal" as the HTT phase, and is consistent with the "less orthorhombic" low temperature structures proposed previously for $La_{2-x}Sr_{x-y}Ba_yCuO_4$ single crystals (Fujita et al., 2002a).

4.4 Critical phenomena at the HTT → MTO phase transition

Previous work on the HTT→MTO phase transition in polycrystalline $La_{2-x}Sr_xCuO_4$ and $La_{2-x}Ba_xCuO_4$ samples show the orthorhombic strain to scale as the square of the order parameter (Birgeneau et al., 1987; Böni et al., 1988; Suzuki and Fujita, 1989a,b). Consequently we examined the critical behaviour of the orthorhombic strain in our $La_{2-x}Ba_xCuO_4$ single crystals by fitting the measured strain as a function of temperature to:

$$\Delta(T) = \Delta_0 \times (\frac{T_{d1} - T}{T_{d1}})^{2\beta} + Background \tag{4.2}$$

where the square of the order parameter, Δ, has been described before (see Equ. 4.1) , and the background accounts for finite strain within the HTT phase introduced by the fitting process described above. The results of this fitting is shown in figure 4.5, which shows the orthorhombic strain as a function of reduced temperature, $(T\text{-}T_{d1})/T_{d1}$, in the region of small reduced temperature close to T_{d1}. Clearly this description of the data is very good. It results in accurate estimates for both β and T_{d1}. These are T_{d1}=232.3 ± 0.7 K, 271.7 ± 1.0 K, and 305.4 K ± 1.0 K for the x=0.125, 0.095, and 0.08 samples, respectively. The extracted values for β are 0.35 ± 0.03, 0.34 ± 0.04 and 0.28 ± 0.06, respectively.

Using these values of T_{d1} for each of the three samples, we can scale the

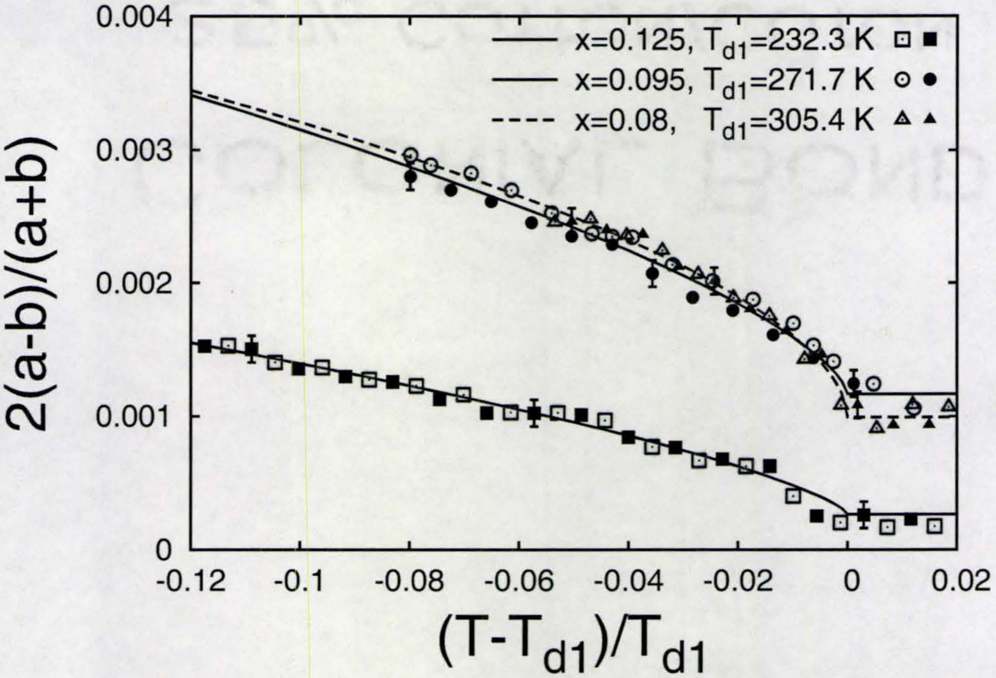

Figure 4.5: The orthorhombic strain is plotted vs reduced temperature, (T-T_{d1}/T_{d1}) for the x=0.125, 0.095, and 0.08 $La_{2-x}Ba_xCuO_4$ samples at small values of reduced temperature, near T_{d1}. The open and filled symbols show data from warming and cooling cycles, respectively. Fits of the data to the form of the order parameter squared vs reduced temperature, Eq. 4.2, used to extract values of β are shown as the solid lines.

plot of orthorhombic strain vs temperature, figure 4.4a, so as to give scaled orthorhombic strain vs T/T$_{d1}$, which is shown in figure 4.4b. We see that above T/T$_{d1}$ $\sim$ 0.8 the orthorhombic strains for all three samples collapse to a single curve. We therefore expect universal behaviour in this regime, which is borne out by the similarity in the extracted values for the critical exponent β at all three Ba concentrations.

The uncertainties associated with the critical exponent β are largely determined by the uncertainties in the critical temperature, T$_{d1}$, derived from the fits to the critical behaviour. We performed fits to Eq. 4.2 using T$_{d1}$ set to a range of values around the approximate phase transition temperature, and then allowed the fit to adjust the other parameters in Eq. 4.2. This gives a monotonically increasing estimate for β as a function of increasing T$_{d1}$. Best estimates for β and T$_{d1}$ are given by the minimum in the goodness-of-fit parameter χ^2 which we define as:

$$\chi^2 = \frac{\sum(\Delta_{measured} - \Delta_{calculated})^2}{N} \tag{4.3}$$

where N is the number of data points.

β and χ^2 are shown as a function of T$_{d1}$ for the x=0.125 (top panel), x=0.095 (middle panel), and x=0.08 (bottom panel) samples in figure 4.6. The uncertainty in β is determined by the corresponding uncertainty in T$_{d1}$, and it is roughly 10% for the x=0.125 and 0.095 samples where we have an extended data set throughout the MTO phase, and roughly 20% for the x=0.08 sample where the data set is restricted to temperatures close to T$_{d1}$.

Investigation of the critical properties at the HTT→MTO phase transition in polycrystalline $La_{2-x}Sr_xCuO_4$(Birgeneau et al., 1987; Böni et al., 1988) and $La_{2-x}Ba_xCuO_4$(Suzuki and Fujita, 1989a,b) anticipated 3D XY universal-

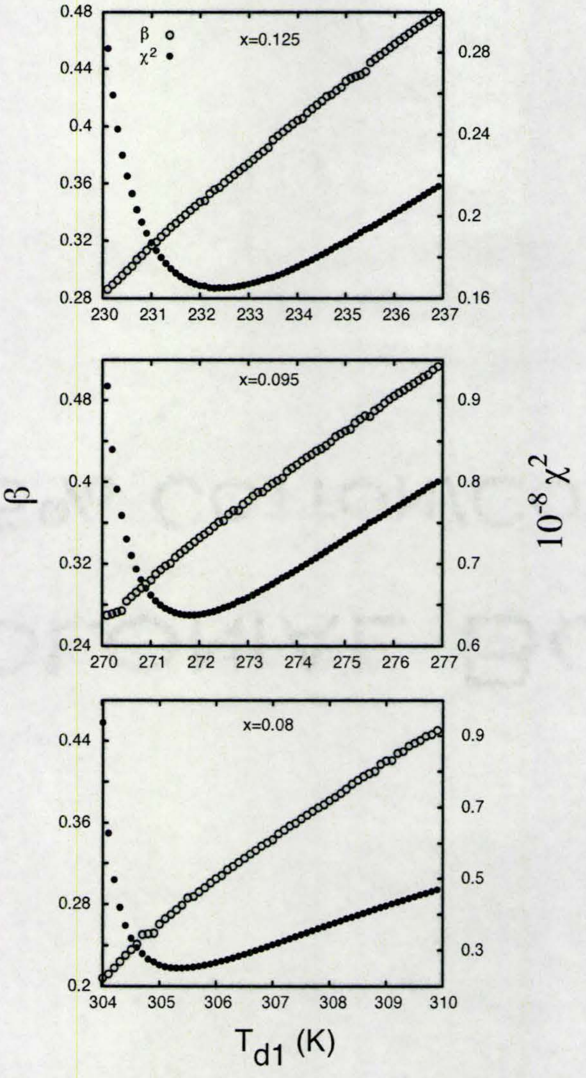

Figure 4.6: The dependence of critical exponent β and goodness-of-fit parameter χ^2 are shown as a function of the assumed value of T$_{d1}$ for x=0.125 (upper panel), x=0.095 (middle panel) and x=0.08 (lower panel) $La_{2-x}Ba_xCuO_4$ single crystal samples. The uncertainty in β is largely determined by the uncertainty in critical temperature T$_{d1}$.

ity on the basis of a Landau expansion appropriate to this ferroelastic system. These early results on polycrystalline systems were consistent with the β=0.35 expected from 3D XY universality (Le Guillou and Zinn-Justin, 1977, 1980). However, these earlier estimates for β spanned the range from 0.28 to 0.37, ignoring uncertainties associated with the estimates, which covers all standard 3D universality classes: Heisenberg ($\sim$0.37), XY ($\sim$0.35), Ising ($\sim$0.32) and which begins to approach values consistent with tricritical phenomena (0.25) (Collins, 1989).

Figure 4.7 shows the orthorhombic strain, 2(a-b)/(a+b), plotted as a function of the reduced temperature, $(T_{d1}-T)/T_{d1}$, on a log-log plot in order to identify the expected power law regime. For comparison a straight line appropriate to β=0.35 and 3D XY universality is also plotted. For each sample, two data sets are plotted, one for a warming run and one for a cooling run. We observe very similar power law behaviour in all three samples, and behaviour which is very much consistent with 3D XY universality as anticipated theoretically. We also see, at least for the x=0.125 and 0.095 samples for which we have data over the entire MTO phase regime in temperature, that a single power law is a remarkably good descriptor of the data over a very large temperature regime. There appears to be a slight increase in slope for reduced temperatures greater than $\sim$ 0.2, but overall, power law-like growth of the orthorhombic strain is observed over almost two decades in reduced temperature. This is in contrast to most critical phenomena, wherein asymptotic critical behaviour is expected to cross over to a mean field-like regime, as one moves away from the critical temperature.

Taken together our orthorhombic strain measurements show critical behaviour at the HTT→MTO phase transition in single crystal $La_{2-x}Ba_xCuO_4$

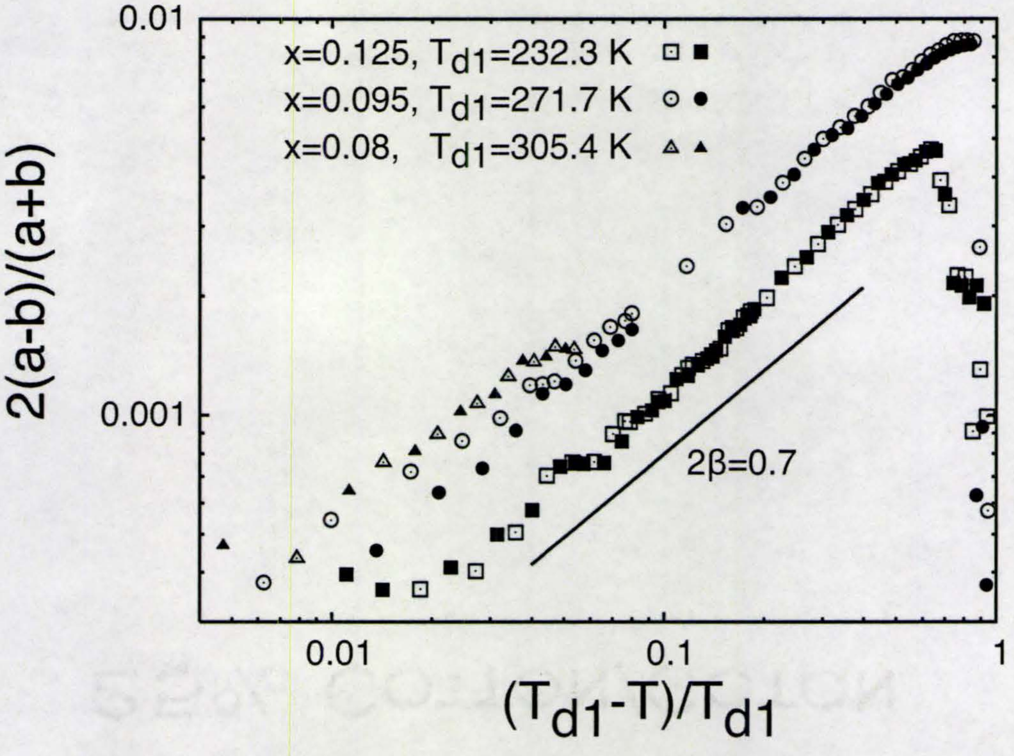

Figure 4.7: The orthorhombic strain is plotted as a function of reduced temperature, $(T_{d1}-T)/T_{d1}$, on a log-log scale for the x=0.125, 0.095 and 0.08 single crystal $La_{2-x}Ba_xCuO_4$ samples. The open and filled symbols show results from warming and cooling cycles, respectively. For comparison power law behavior showing β=0.35, indicative of the theoretically expected 3D XY universality class, is indicated as the straight line on this log-log plot.

over a broad range of concentration which is characterized by β=0.34 ± 0.04. This result clearly demonstrates 3D universality, and is consistent with 3D XY universality which is expected based on Landau theory. It is also largely consistent with previous experimental work on single crystal and polycrystal $La_{2-x}Sr_xCuO_4$ and polycrystalline $La_{2-x}Ba_xCuO_4$, much of which centred on measurements of superlattice Bragg peak intensities within the MTO structure, as opposed to measurements of the orthorhombic strains (Braden et al., 1994; Thurston et al., 1989). Superlattice Bragg peak intensities near continuous phase transitions can be difficult to interpret, as they can be influenced by extinction and by fluctuations above the phase transition. This latter effect manifests itself in upwards curvature and difficulty identifying a precise phase transition temperature, which in turn can lead to uncertainty in critical exponents.

4.5 Phase diagram and comparison to polycrystalline materials

It is of interest to compare the $La_{2-x}Ba_xCuO_4$ phase diagram known to characterize pre-existing polycrystalline samples (See Fig 1.1b)with that determined for the high quality single crystals in the present studies. A rather detailed comparison can be carried out, as two structural and one superconducting transition temperature characterize $La_{2-x}Ba_xCuO_4$ samples in this underdoped concentration range. The phase transitions measured for the single crystals in this study are summarized in Table 4.1. The critical exponent β relevant to the HTT→MTO structural transition is also shown in the same table for reference.

Table 4.1: Summary of structural and superconducting phase transition temperatures in single crystal $La_{2-x}Ba_xCuO_4$

x	T_{d1}(K)	T_{d2}(K)	T_c(K)	β
0.125	232.3	60	4 [1]	0.35 ± 0.03
0.095	271.7	45 [2]	27 [2]	0.34 ± 0.04
0.08	305.4	35 [2]	29 [2]	0.28 ± 0.06

[1] From Ref. (Fujita et al., 2004)

[2] From Ref. (Dunsiger et al., 2008a)

The superconducting transition temperatures were determined from SQUID magnetometry as described in Chapter 2 for the x=0.095 and x=0.08 samples, and reported by Fujita et al. (Fujita et al., 2004) for the x=0.125 sample. The strongly first order MTO→LTT transition is measured both by the abrupt change in the orthorhombic strain seen in figure 4.2 and 4.3, for the x=0.125 and x=0.095 samples, respectively, as well as by the appearance of the (0, 1, 0) superlattice Bragg peak intensity (See Chapter 5) for the x=0.095 and x=0.08 samples, and as reported by Fujita et al. for the x=0.125 sample (Fujita et al., 2004).

Figure 4.8 shows the $La_{2-x}Ba_xCuO_4$ phase diagram with HTT, MTO, and LTT phases indicated. The HTT→MTO and MTO→LTT transitions are shown as filled squares for the three Ba concentrations measured. The discontinuous transition at T_{d2} is indicated as a bar, in order to show the onset to completion of the transition, which is $\sim$ 10 K wide. T_{d2} in Table 4.1 is the midpoint of the transition. The superconducting transitions are given by the open circles, and they indicate the onset of the superconductivity, which is also what is listed in Table 4.1. Previous results for these same phase boundaries as determined for polycrystalline $La_{2-x}Ba_xCuO_4$ samples are shown as the solid lines in figure 4.8. These results were extracted from Adachi et al. (Adachi et al., 2001) and are reproduced here.

As can be seen on inspection of figure 4.8, the agreement between the structural and superconducting phase boundaries in polycrystalline samples of $La_{2-x}Ba_xCuO_4$ and the new floating zone image furnace grown single crystals is remarkably good. The absolute values for T_{d2} are systematically high, at the 10% level for the polycrystalline materials as compared to the single crystals, but overall the full level of agreement is excellent. In particular we see that good agreement between the two for T_{d1} means that this transition can be used as an accurate marker for the Ba concentration in single crystal $La_{2-x}Ba_xCuO_4$, as T_{d1} has such strong Ba dependence. The image furnace single crystals were grown without crucibles, and are expected to be of higher purity than the corresponding polycrystalline materials grown from a flux melt in a crucible. The similarity between the overall phase diagrams in polycrystalline and image furnace grown single crystal $La_{2-x}Ba_xCuO_4$, implies an insensitivity of these phase boundaries to this level of imperfection.

4.6 Orthorhombic strain vs. Ba concentration

For more highly doped $La_{2-x}Ba_xCuO_4$ materials (x=0.125, 0.095 and 0.08), T_{d1} associated with T_{d2} and T_c are perfect markers for doping levels. However, with decreased Ba concentration, especially when $x < 0.05$, the T_{d1} is much higher than room temperature. Measuring T_{d1} is much more difficult

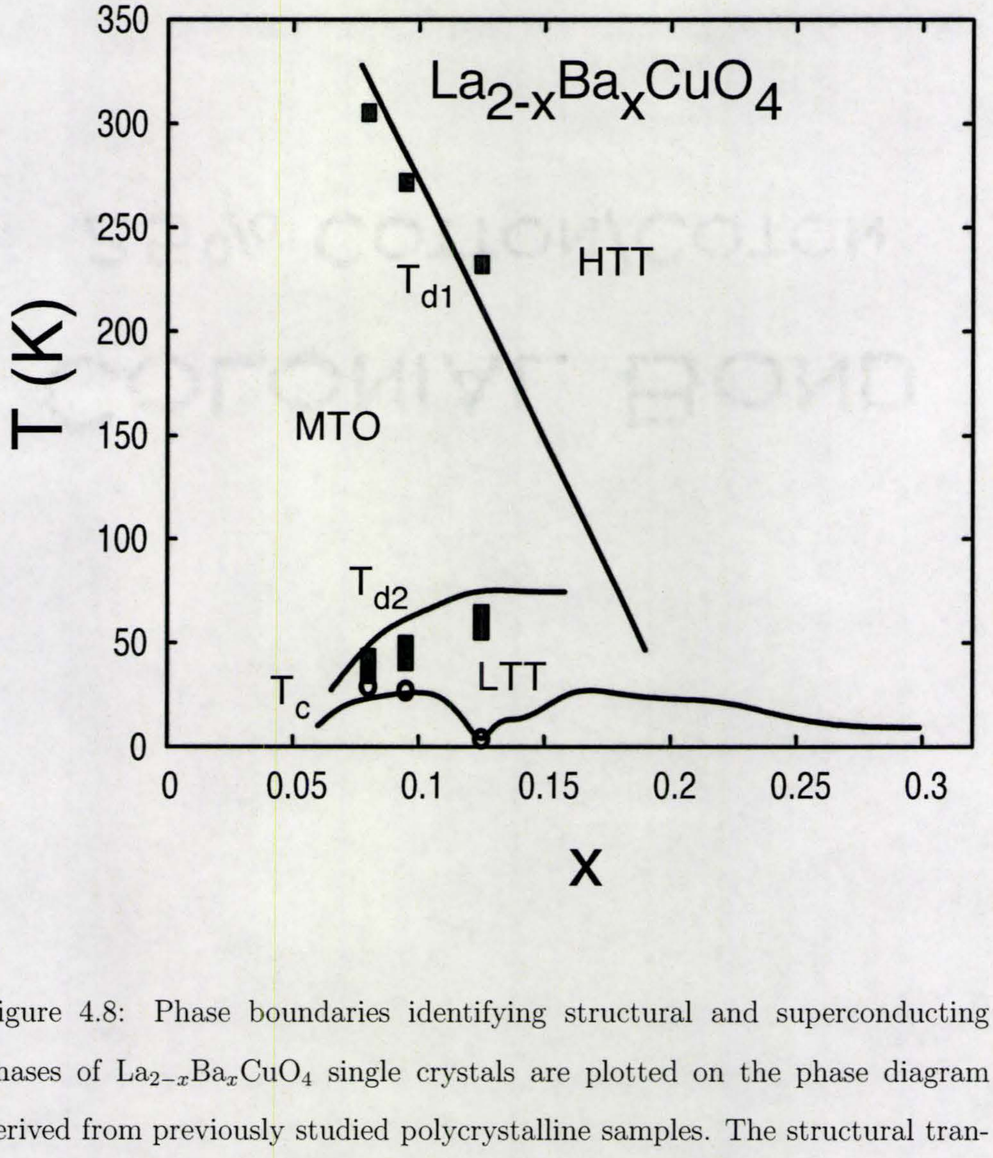

Figure 4.8: Phase boundaries identifying structural and superconducting phases of $La_{2-x}Ba_xCuO_4$ single crystals are plotted on the phase diagram derived from previously studied polycrystalline samples. The structural transitions at T_{d1} and T_{d2} are indicated by filled squares, while superconducting T_C's are indicated by open circles. The first order transition at T_{d2} is indicated by a bar ~ 10 K wide, showing the onset to completion of the phase transition. Solid lines showing phase boundaries from polycrystalline $La_{2-x}Ba_xCuO_4$ are taken from Adachi et al. (Adachi et al., 2001)

using normal sample environments. In addition, with doping levels moving out of the superconductivity dome, LTT phase also disappear, which indicate the absence of T_{d2} and T_c as shown in figure 4.8.

In Section 4.3, we found that the orthorhombic strain, 2(a-b)/(a+b), in the x=0.125 sample is much smaller than x=0.095 sample. This result suggests that the orthorhombic strain is also doping dependent, and it can be used as another calibration of doping levels. In fact, the orthorhombic strain is more suitable at lower Ba concentrations. Combining both X-ray and neutron diffraction data, we can plot the maximum orthorhombic strain as the function of doping levels x and this is shown in figure 4.9. For the $x \leqslant 0.05$ samples, we calculate the orthorhombic strain using the $(1, 1, 0)_{HTT}$ Bragg reflection obtained with neutron diffraction data at the lowest temperature we could reach (See chapter 5). For higher doping samples, we use the data sets collected in the MTO phase and just above the T_{d2}. The undoped La_2CuO_4 data point is taken from literature (Kastner et al., 1998). Compared to the linear relation between the orthorhombic strain and Sr concentration in the $La_{2-x}Sr_xCuO_4$ system (Fujita et al., 2002b) (See figure 4.9 open circle and dash line), we see the doping dependence of the orthorhombic strain in the $La_{2-x}Ba_xCuO_4$ system is slightly curved downwards as the doping increases. This result may be due to the orthorhombic strain not being fully developed in $La_{2-x}Ba_xCuO_4$due to the presence of the LTT phase. Nevertheless, we can estimate the magnitude of Ba concentration using the orthorhombic strain. It is also interesting to note that the superconducting transition temperatures display a similar trend as the orthorhombic strain as a function of doping, as shown in figure 4.8. The dividing point near x=0.125 probably indicates a significant change in the nature of the superconducting ground state near this

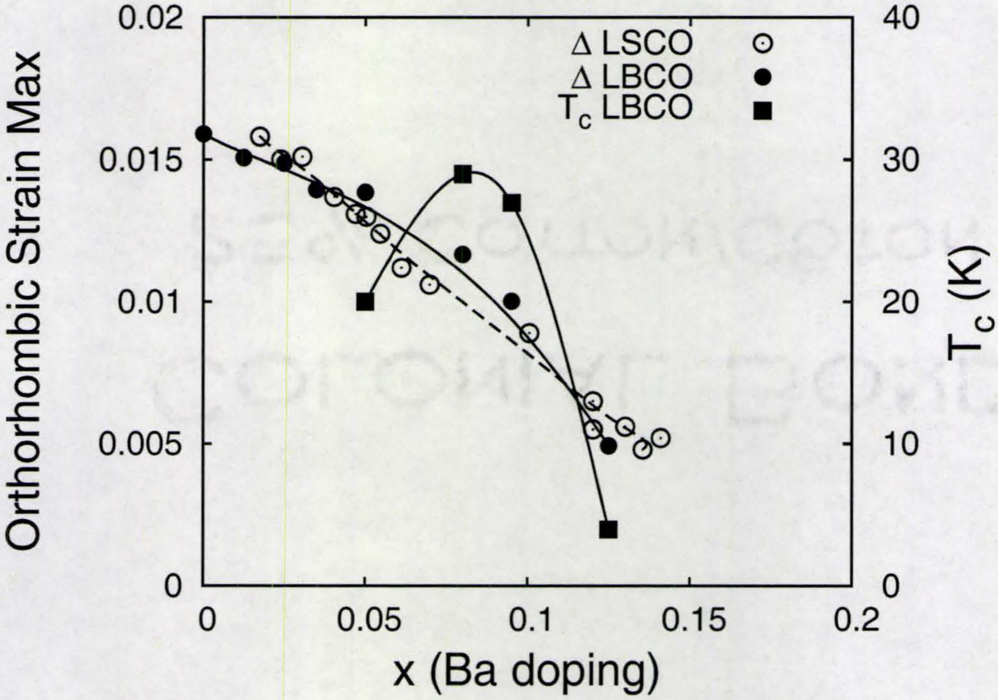

Figure 4.9: Orthorhombic strain maximum in $La_{2-x}Ba_xCuO_4$ and $La_{2-x}Sr_xCuO_4$ (closed and open circles, respectively) and superconducting transition temperature in $La_{2-x}Ba_xCuO_4$ (close square) as a function of doping. The x=0.125, 0.095 and 0.08 data was taken from X-ray measurements discussed in this chapter. Lower concentrations employed neutron scattering data. The solid line is a guide to the eye. The $La_{2-x}Sr_xCuO_4$ data is taken from Fujita *et al.* (Fujita et al., 2002b). The dash line indicates the linear relation between the orthorhombic strain and the doping levels in $La_{2-x}Sr_xCuO_4$ system

concentration.

4.7 Discussion

High resolution single crystal x-ray diffraction measurements were carried out on x=0.08 and 0.095, as well as on a high quality x=0.125 single crystal. These measurements focused on the $(3, 3, 0)_{HTT}$ Bragg peak and showed the evidence of the HTT→MTO→LTT sequence of structural phase transitions known to be relevant to underdoped $La_{2-x}Ba_xCuO_4$. The measurements also clearly show anomalous longitudinal broadening of the $(3, 3, 0)_{LTT}$ Bragg peaks in the x=0.095 and x=0.125 samples at low temperatures, indicating that the LTT phase is not a simple tetragonal phase, but rather an admixture of tetragonal and orthorhombic phases, or an orthorhombic phase with very small orthorhombic strain. Critical orthorhombic strain measurements near the continuous HTT→MTO phase boundary show clear 3D universality, with universal behavior observed in the orthorhombic strain vs T/T_{d1} for the three x=0.125, 0.095 and 0.08 samples. The best estimate for a common critical exponent β for these samples is $\beta=0.34 \pm 0.04$, which is consistent with 3D XY universality expected theoretically for such ferroelastic transitions. A detailed comparison of the $La_{2-x}Ba_xCuO_4$ phase diagram incorporating structural and superconducting phase boundaries at this underdoped concentration regime indicates excellent agreement with pre-existing data based on polycrystalline samples. Using both X-ray and neutron diffraction data, we have calculated the maximum orthorhombic strain in these samples as a function Ba concentration. This result can be used to estimate the Ba concentration in the lightly doped range of $La_{2-x}Ba_xCuO_4$ materials, where it is difficult to estimate from structural and superconducting transition temperatures.

Chapter 5

Neutron scattering studies of underdoped $La_{2-x}Ba_xCuO_4$

5.1 Introduction

This chapter discusses neutron scattering results on underdoped single crystals of $La_{2-x}Ba_xCuO_4$. We performed neutron scattering measurements on x=0.095, 0.08, 0.05 and 0.025 samples. The purpose of this study was to measure the incommensurate magnetic structure in $La_{2-x}Ba_xCuO_4$ single crystals with different doping levels and to investigate the evolution of magnetism as function of doping in the underdoped $La_{2-x}Ba_xCuO_4$ system.

These results show that high temperature superconducting samples of $La_{2-x}Ba_xCuO_4$ with x=0.095 and 0.08, show static incommensurate spin ordering developing along the "collinear" direction below similar temperature $T_N \sim 39$ K within low temperature tetragonal phase. The incommensurate spin orderings in both samples is insensitive to the onset of superconductivity. More surprisingly, the spin ordering in the x=0.095 sample is shown to be insensitive to application of an external magnetic field up to 7 T applied along c-axis. Such magnetic field independent behaviour is in marked contrast to the magnetic field enhanced and induced incommensurate spin ordering with similarly doped $La_{2-x}Sr_xCuO_4$ samples (Lake et al., 2002). In addition dispersive spin excitations are observed in $La_{2-x}Ba_xCuO_4$, x=0.095, at the same incommensurate wavevector as describes the long range order and these persist above 60 K. The associated dynamical spin susceptibility of the low energy spin excitations is seen to saturates below T_c.

Neutron measurements were also performed on lightly doped samples of $La_{2-x}Ba_xCuO_4$, corresponding to x=0.025 and 0.05, where we observe the incommensurate spin ordering to rotate by 45°, with respect to the ordering within the x=0.095 and 0.08 superconducting samples, to lie along the "diagonal" direction at low temperature. Such a rotation in the orientation of the static spin ordering as a function of increasing Ba concentration, from diagonal to collinear, is roughly coincident with the transition from an insulating to a superconducting ground state. This effect is similar to that observed in well studied $La_{2-x}Sr_xCuO_4$ system (Matsuda et al., 2000), indicating that this phenomenon is a more generic property of underdoped La-214 cuprates. However, the incommensurate wavevector δ show different Ba doping dependence in these two regimes. δ is seem to be only weakly dependent on the Ba doping in the superconducting regime, different from the behaviour seen in $La_{2-x}Sr_xCuO_4$ superconductors. At lower doping levels, δ is proportional to Ba concentration as was also the case in the $La_{2-x}Sr_xCuO_4$ materials in this doping range.

In order to maintain a consistent definition of δ value, we use the HTT unit cell, square lattice, notation throughout our discussion, where $a \simeq b \sim 3.78$

Å and c = 13.27 Å. The results reported in this chapter have been published in the scientific literature (Dunsiger et al., 2008a) or are in preparation.

5.2 Neutron scattering studies in the superconducting regime of $La_{2-x}Ba_xCuO_4$

Neutron scattering experiments on the $La_{2-x}Ba_xCuO_4$ superconducting samples with x=0.095 and 0.08, were carried on using the C5 and N5 triple axis spectrometers and the thermal neutron source at the Canadian Neutron Beam Center, Chalk River Laboratory. All experiments performed at Chalk River were used pyrolytic graphite (002) planes as both monochromator and analyzer, and a with constant E_f=14.7 meV was employed in all measurements . A pyrolytic graphite filter was placed in the scattered beam to reduce contamination from higher order neutrons. The detailed configurations used in these experiments are listed in Table 3.1

5.2.1 Elastic neutron scattering results

We first discuss the elastic neutron scattering measurements of incommensurate magnetic Bragg peaks in $La_{2-x}Ba_xCuO_4$ with x=0.095 and 0.08 single crystals. The samples were initially oriented with the $(hk0)$ reciprocal space plane coincident with the horizontal scattering plane. Figure 5.1 shows elastic neutron scattering scans along the h direction at T=3.8 K and along the k direction at 8 K in the x=0.095 and 0.08 single crystals, respectively. The incommensurate magnetic Bragg peaks appear at $(0.5\pm\delta, 0.5, 0)$ for the x=0.095 sample and at $(0.5, 0.5\pm\delta, 0)$ for the x=0.08 sample. Analogous magnetic peaks are also observed at (0.5, 0.5$\pm\delta$, 0) for x=0.095 and at (0.5$\pm\delta$, 0.5, 0) for x=0.08. These incommensurate magnetic peaks as shown in figure 5.1 were fit to a Lorenzian form

$$S(Q) = \frac{A}{\pi}\frac{\kappa}{[Q-(0.5\pm\delta)]^2+\kappa^2} + Background \tag{5.1}$$

where δ is incommensurate wave-vector and κ is half width at half maximum (HWHM), which is inverse of the correlation length within the basal plane. All peaks widths were resolution limited with δ=0.112(3), κ=0.0055 Å^{-1} (x=0.095) and δ=0.107(3), κ=0.0063 Å^{-1} (x=0.08). The corresponding static spin correlation lengths within the basal plane exceed 180 Å for x=0.095 and 158 Å for x=0.08 samples. The value of δ decreases as the Ba concentration is reduced in $La_{2-x}Ba_xCuO_4$ system as we expected. However the doping dependence of δ is weaker in our samples of $La_{2-x}Ba_xCuO_4$ compared to $La_{2-x}Sr_xCuO_4$ with similar doping levels.

The temperature dependence of the elastic incommensurate magnetic peaks and (0, 1, 0) superlattice structural Bragg peaks in x=0.095 and 0.08 samples are shown in figure 5.2 and 5.3, respectively. The intensity of the magnetic Bragg peak is proportional to the volume average of the square of the ordered staggered magnetic moment as we discussed in Chapter 3. The (0, 1, 0) superlattice structural Bragg peak is indicative of the orthorhombic to low temperature tetragonal phase transition (T_{d2}), which is discontinuous in nature (Axe et al., 1989a) and has been discussed in Chapter 4. Figure 5.2 shows that the spin order at (0.612, 0.5, 0) (x=0.095) develops continuously with temperature below T_N=39.5$\pm$0.3 K with T_{d2} $\sim$45 K. For reference, the superconducting transition at T_c $\sim$27 K is also indicated on the figure as a dashed line. Similar to our results on the x=0.095 sample, we see that the

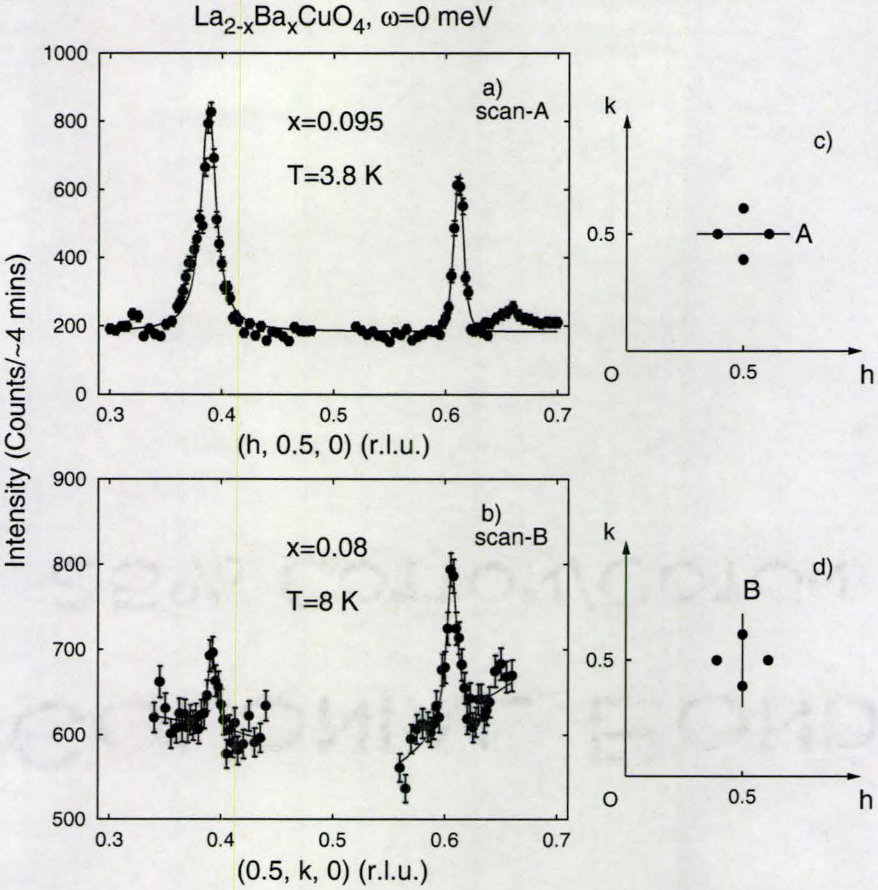

Figure 5.1: (a)Static incommensurate magnetic peaks with δ=0.112(3) in $La_{2-x}Ba_xCuO_4$ x=0.095 at 3.8 K, along (h, 0.5, 0) as shown in (c). (b) Similar static incommensurate magnetic peaks with δ=0.107(3) in $La_{2-x}Ba_xCuO_4$ x=0.08 at 8 K, along (0.5, k, 0) as shown in (d). The solid line in (a) and (b) are fitting results using a Lorenzian profile as described in text.

spin order at (0.5, 0.607, 0) in our x=0.08 sample develops continuously below T_N ~39 K with T_{d2} ~35 K as shown in figure 5.3. For both samples, the onset of spin ordering, T_N correlates most strongly with the completion of the transition to the low temperature tetragonal phase, and the incommensurate spin order coexists with the superconductivity below T_c. Associated incommensurate charge ordering has not been observed. The temperature dependence of the spin ordering is qualitatively similar to that observed in the x=1/8 compound (Fujita et al., 2004), where the superlattice peak intensity becomes non-zero below ~ 50 K.

A comparison of the magnetic Bragg peaks intensity in the x=0.095 and 0.08 samples, as shown in figure 5.1, 5.2 and 5.3, shows that the scattered intensity is much weaker in the x=0.08 sample than in the 0.095 sample. In order to directly compare the temperature dependence of the two samples, we need to scale the magnetic peak intensities with their sample volumes. We can use either the integrated intensity of an acoustic phonon near a strong nuclear Bragg peak or the supperlattice structural Bragg peak intensity to calculate the volume fraction. During this study, we collected inelastic phonon scattering at (2, 0.15, 0) and obtained a ratio of sample volumes $V_{0.095}$:$V_{0.08}$ ~1:1.2. This ratio is also similar to the value given by the (0, 1, 0) peak intensities. Figure 5.4 a) shows the magnetic Bragg peak intensity in the x=0.095 and 0.08 samples scaled by their volume ratio. Surprisingly, the magnetic scattering in the x=0.08 sample is roughly a factor of four less intense than that of the x=0.095 sample. We do not understand the reduced magnetic Bragg intensity for the x=0.08 sample. Extinction does not play a role. Such a reduction in the elastic magnetic scattering also implies that the associated inelastic scattering signal is prohibitively weak to be observed. We also plot

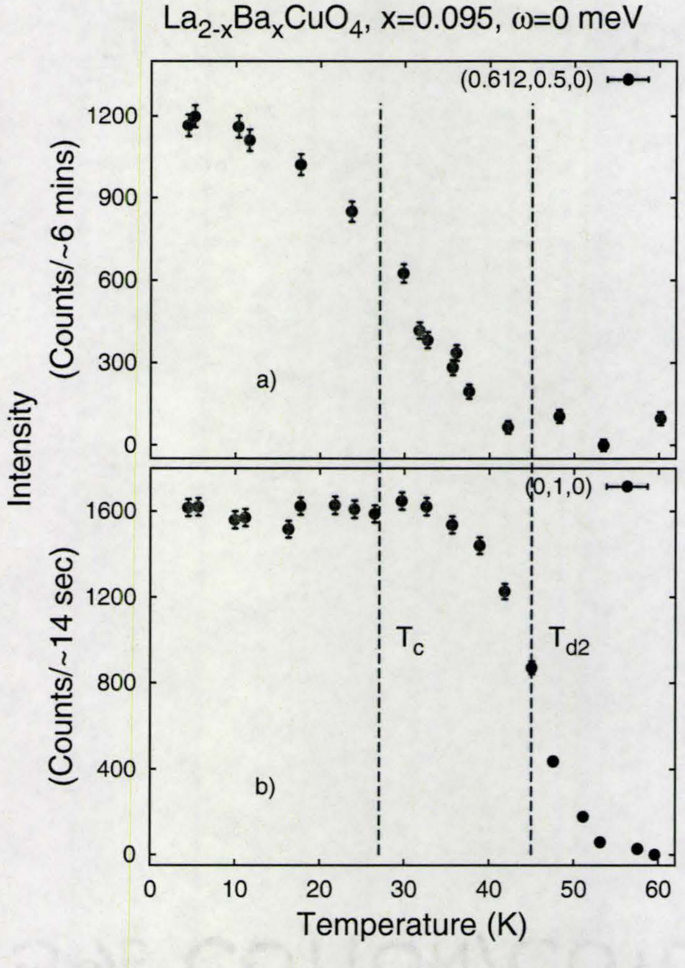

Figure 5.2: a)The temperature dependence of the net elastic incommensurate magnetic scattering in $La_{2-x}Ba_xCuO_4$, x=0.095, at (0.612,0.5,0), as well as that of b) the (0,1,0) structural Bragg peak, which marks the orthorhombic to low temperature tetragonal structural phase transition. Note that a constant background has been subtracted in both cases. The superconducting, T_c, and structural phase transition, T_{d2}, temperatures are indicated by dashed lines.

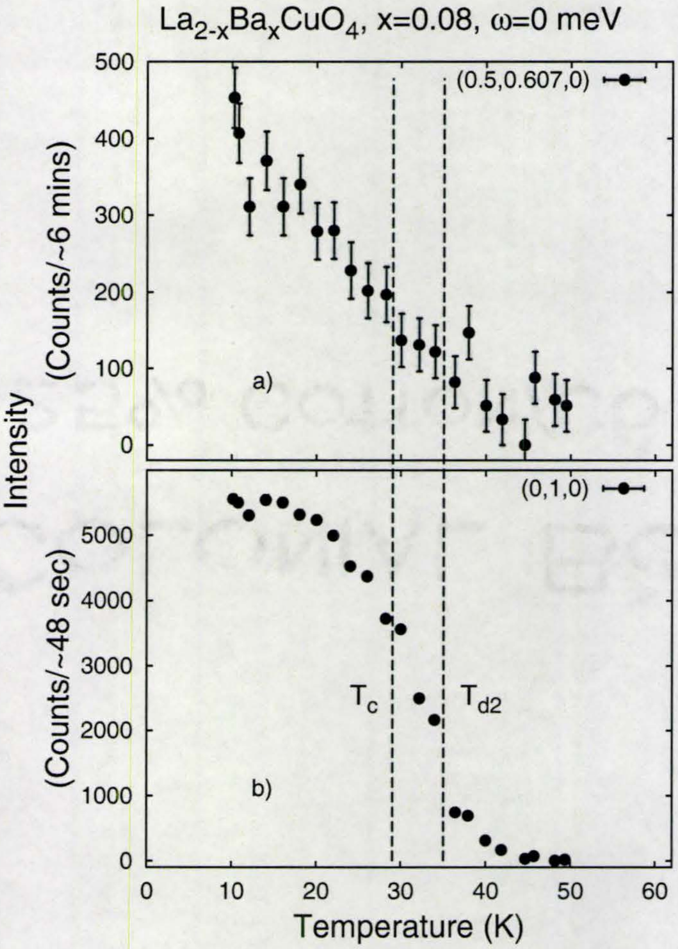

Figure 5.3: a)The temperature dependence of the net elastic incommensurate magnetic scattering in $La_{2-x}Ba_xCuO_4$, x=0.08, at (0.5,0.607,0), as well as that of b) the (0,1,0) structural Bragg peak, which marks the orthorhombic to low temperature tetragonal structural phase transition. Note that a constant background has been subtracted in both cases. The superconducting, T_c, and structural phase transition, T_{d2}, temperatures are indicated by dashed lines.

normalized peak intensities in both samples so that their functional form may be directly compared (See figure 5.4 b). As can be seen, both the temperature dependence of the order parameter and the phase transition temperatures are very similar despite the difference in the strength of the elastic magnetic Bragg scattering. We therefore conclude the two electronic energy scales for these crystals at x=0.08 and x=0.095, set by the superconducting T_c and T_N, are surprisingly similar. It is not clear why a 4% decrease in δ should produce an four-fold decrease in the magnetic Bragg intensity. One possibility was that the ordering in the x=0.08 sample was beginning to develop in the diagonal directions, however a search revealed no additional magnetic intensity in diagonal directions.

An interesting difference between the $La_{2-x}Ba_xCuO_4$ single crystal samples with x=0.08 and x=0.095 is that the spin ordered state in the x=0.095 sample grows within a fully developed LTT structure, as $T_N \sim 39.5$ K and $T_{d2} \sim$ 45 K. By contrast, in the x=0.08 $La_{2-x}Ba_xCuO_4$ sample, the MTO to LTT structural phase transition begins near T_N on decreasing temperature and is only completed at temperatures below $\sim$ 20 K. The situation for x=0.125 $La_{2-x}Ba_xCuO_4$ is similar to the x=0.095 case, as $T_N \sim$ 50 K, at which temperature the MTO-LTT transition for x=0.125 is largely complete. The first order nature of the MTO-LTT structural phase transition implies coexisting structures over the temperature regime at which the spin order forms for x=0.08 $La_{2-x}Ba_xCuO_4$. It is then possible that the resulting structural heterogeneity interferes with the full development of spin order, giving rise to a substantially reduced magnetic Bragg intensity as compared with the x=0.095 sample. However, we also note that variability (Lake et al., 2002) in the elastic magnetic Bragg intensity has been reported from $La_{2-x}Sr_xCuO_4$ sample to sample with

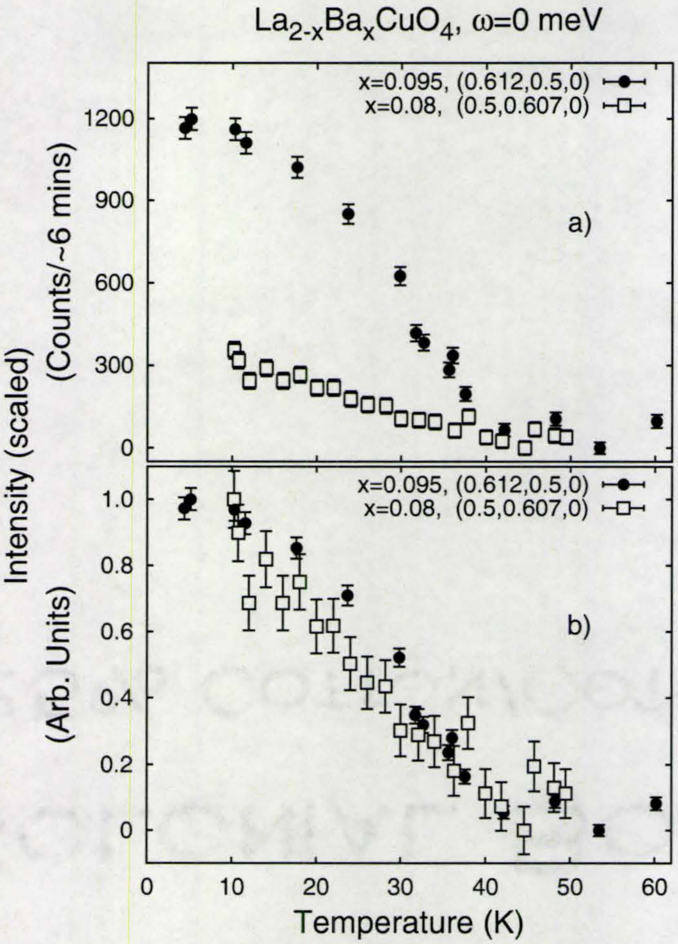

Figure 5.4: The temperature dependence of the net elastic incommensurate magnetic scattering in $La_{2-x}Ba_xCuO_4$, x=0.095 at (0.612, 0.5, 0) (closed circle) and x=0.08, at (0.5,0.607,0) (open square). a) The intensity has been scaled by the phonons collected near a strong Bragg peak at (2, 0.15, 0) in both samples. b) The intensity has been normalized to that at the lowest temperature.

similar nominal doping levels of x$\sim$ 0.1 and the $La_{2-x}Sr_xCuO_4$ system does not display the LTT phase at low temperatures.

Unlike the long range correlations within CuO_2 planes, the inter-plane correlations are very short, which give rods like magnetic scattering extending out of the $(h, k, 0)$ plane from the magnetic incommensurate positions. To observe this scattering along L, the crystal was reoriented in the (h, h, l) scattering plane and then tilted $\sim 7°$ at constant L to intersect the incommensurate peak position for h=0.39. Measurements along the solid line illustrated in figure 5.5 b) of the form $(h, h/(1-2\delta), l)$ at fixed L for L=2, 2.25, 2.5 and 3 are shown in figure 5.5 a) at T=3.5 K and at L=3 for T=50 K to extract a background. Since the peak intensity is independent of L, the scattering taking the form of an elastic rod along the L direction, the static spin order at low temperatures is two dimensional. Note that the intensity in figure 5.1 a) is greater relative to that in figure 5.5 a) for the sample oriented in the $(h, k, 0)$ plane. This arises because the neutron spectrometer has a broad vertical resolution which integrates the signal in the L direction, perpendicular to the scattering plane.

5.2.2 Magnetic field effects on incommensurate spin order in the single crystal of $La_{2-x}Ba_xCuO_4$ with x=0.095

One of the most surprising results of this study is that the incommensurate spin structure shows no magnetic field dependence up to 7 T, applied vertically along the c* axis. Neither cooling nor warming the sample in a magnetic field has an effect on either the temperature dependence of the spin

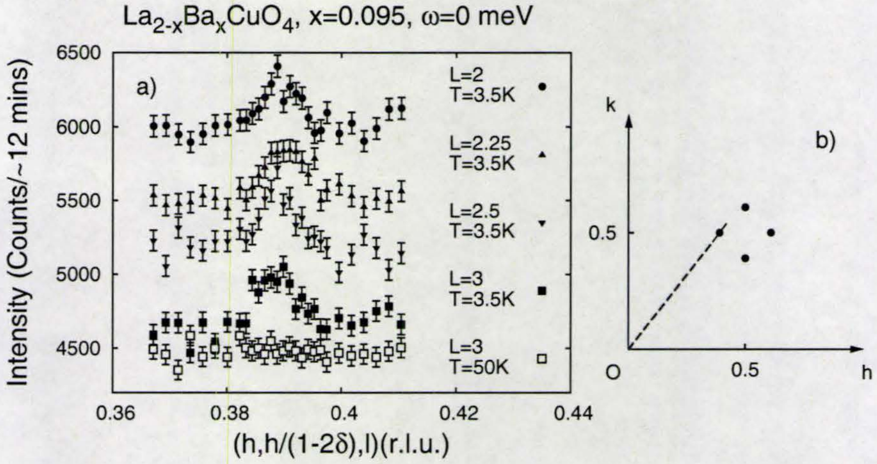

Figure 5.5: a) Elastic scans of the form $(h, h/(1-2\delta), l)$, as shown with the solid line in b), which demonstrate the rod-like, two dimensional nature of the elastic magnetic scattering, as described in the text. The scans have been displaced by 300 counts upwards for clarity. The dashed line in b) illustrates that the scattering plane is slightly miss-set from the $(h, k, 0)$ plane and passes throughout one of the incommensurate magnetic Bragg peaks

ordering, or the Bragg intensity in $La_{2-x}Ba_xCuO_4$,x=0.095, as shown in figure 5.6. This result is in marked contrast with the behaviour of underdoped and optimally doped $La_{2-x}Sr_xCuO_4$ where pronounced field dependent effects are observed.

For underdoped $La_{2-x}Sr_xCuO_4$ (x=0.12,0.10), the ordered magnetic moment associated with preexisting static spin order is enhanced on application of a magnetic field (Katano et al., 2000; Lake et al., 2002, 2005). The spin order within the vortex state of $La_{2-x}Sr_xCuO_4$ (x=0.10) (Lake et al., 2002) indicates long in-plane correlation lengths, greater than both the superconducting coherence length and the intervortex spacing at the maximum magnetic field employed in this type of study, 14.5 T. As the coherence length is a measure of the size of the vortices, Lake *et al* argued the static magnetism must therefore reside beyond the extent of the vortices themselves (Lake et al., 2002). Whereas the $La_{2-x}Ba_xCuO_4$ (x=0.095) correlation length for static spin order which we measured is similarly long, the underlying physics is clearly different and the spins appear to order independent of vortex creation.

For the optimally doped $La_{2-x}Sr_xCuO_4$ compound (x=0.163), the application of a magnetic field enhances the dynamical spin susceptibility but does not induce static order (Lake et al., 2001). Most dramatically, in a slightly underdoped sample (x=0.144), Khaykovich *et al.* (Khaykovich et al., 2005) report the development of a static incommensurate spin structure above a critical field of 2.7 T. The authors therefore argue that $La_{2-x}Sr_xCuO_4$ (x=0.144) may be tuned through a quantum critical point, at which there is a magnetic field induced transition between magnetically disordered and ordered phases. Their results are interpreted in terms of a Ginzburg-Landau model due to Demler *et al* (Demler et al., 2001), which assumes a microscopic competition between

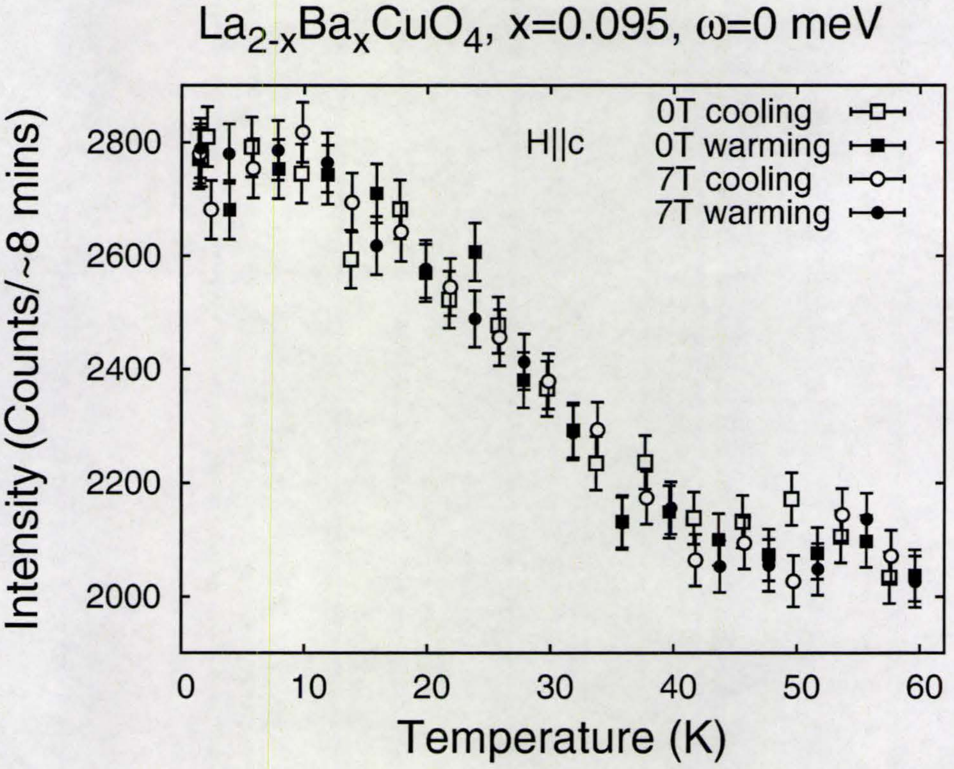

Figure 5.6: Temperature dependence of the elastic incommensurate magnetic scattering in $La_{2-x}Ba_xCuO_4$, x=0.095, at (0.611, 0.5, 0) within H=0 and 7 T $\parallel$ c.

spin and superconducting order parameters. The predicted magnetic intensity increases as $\Delta I \sim H/H_{c2}\ln(H_{c2}/H)$ (Demler et al., 2001), which is consistent with experiments on $La_{2-x}Sr_xCuO_4$. Note that the intensity changes most rapidly with magnetic field at low fields on a scale set by H_{c2}. In the $La_{2-x}Ba_xCuO_4$ family of compounds, the lower critical field is $H_{c1} \sim 0.04$ T, while the upper critical field H_{c2} is in excess of 40 T (Takagi et al., 1987). The upper critical field is of the same order of magnitude in optimally doped $La_{2-x}Sr_xCuO_4$(Boebinger et al., 1996). Thus an applied magnetic field of 7 T should be sufficiently large to have seen such an effect in $La_{2-x}Ba_xCuO_4$.

Whether magnetism and superconductivity coexist in the same microscopic regions of the CuO_2 planes or are phase separated is a topical subject of research. The issue of microscopic spatial segregation has been examined using a combination of neutron scattering (Khaykovich et al., 2002) and μSR (Savici et al., 2002) techniques in La_2CuO_{4+y}. As a local probe μSR is sensitive to heterogeneous structures. The magnetic ordering in $LaCuO_{4+y}$ (y=0.11) and $La_{2-x}Sr_xCuO_4$ (x=0.12) has been reported to occur in reduced magnetic volume fractions of 40 and 18% respectively (Savici et al., 2002). Khaykovich *et al* argued that an applied magnetic field enhances the spin ordering primarily in the nonmagnetic regions (Khaykovich et al., 2002), consistent with the above observations. We speculate that no magnetic field dependence has been observed in $La_{2-x}Ba_xCuO_4$ x=0.095 because the non-magnetic volume fraction is too low. A systematic study of the variation of the spin ordering with magnetic field is therefore of interest, with emphasis on the correlations between this effect and the magnetic volume fraction.

5.2.3 Inelastic magnetic neutron scattering from single crystal $La_{2-x}Ba_xCuO_4$ with x=0.095

The magnetic excitations were studied using constant energy transfer neutron scattering scans performed through the incommensurate ordering wavevectors. Horizontal collimation sequences of 0.54°-0.48°-S-0.54°-1.2° and 0.54°-0.79°-S-0.85°-2.4° were used at energy transfers of 2.07 and 3.1 meV respectively (see Table 3.1, yielding corresponding energy resolutions of ~ 1 and ~ 1.5 meV full width at half maximum (FWHM). The representative scan along $(h, 0.5, 0)$ and $\hbar\omega$=2.07 and 3.1 meV at T=25 K in figure 5.7 a) and b), respectively, show that the low energy dynamic spin response peaks up at the same wave-vector, (0.5±0.112, 0.5, 0), as the static spin structure. At higher energy transfers the signal declines rapidly. The measured dynamic structure factor $S(Q, \omega)$ is related to the imaginary part of the dynamical susceptibility $\chi''(\mathbf{Q}, \omega)$ through the fluctuation-dissipation theorem as we discussed in Chapter 3. For quantitative analysis, the data have been fit to the resolution convolution of

$$S(Q, \omega) = \frac{\chi''(Q, \omega)}{1 - \mathrm{e}^{-\hbar\omega/\mathrm{k_B T}}} \tag{5.2}$$

where the susceptibility (Fujita et al., 2004) is:

$$\chi''(Q, \omega) = \chi''(\omega) \sum_{n=1}^{4} \frac{\kappa}{(Q - Q_{\delta,n})^2 + \kappa^2} \tag{5.3}$$

and $Q_{\delta,n}$ represents the four incommensurate wave vectors $(0.5 \pm \delta, 0.5, 0)$ and $(0.5, 0.5 \pm \delta, 0)$. This assumes the magnetic excitations consist of four rods of scattering running along the c* axis.

The temperature dependences of fitting parameters $\chi''(\omega)$, δ and κ are plotted in figures 5.8 a), b) and c) respectively. $\chi''(\omega)$ is proportional to the

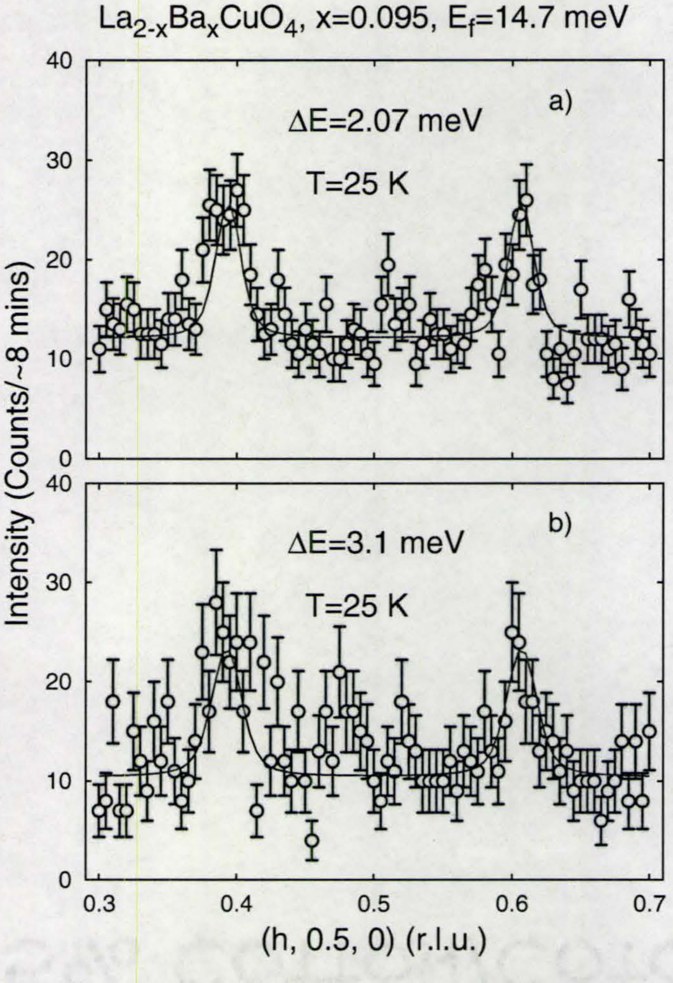

Figure 5.7: a) Representative inelastic scans at T=25 K, also along (H, 0.5, 0) and at $\hbar\omega$=2.07 meV and b) $\hbar\omega$=3.1 meV. The solid lines are the results of fitting the data as discussed in the text.

integral of $\chi''(\mathbf{Q},\omega)$ over $\mathbf{Q}$ in the $(h,k,0)$ scattering plane; δ and κ use the same definitions as we discussed for elastic magnetic scattering. For reference, both the spin ordering transition at $T_N\sim$ 39.5±0.3 K, and the superconducting transition near $T_c\sim$ 27 K are indicated as dashed lines on this plot. At both 2.07 meV and 3.1 meV, the dynamical susceptibility, $\chi''(\omega)$, increases continuously as the temperature is reduced below $\sim$ 60 K, becoming roughly constant and non-zero below $T_C \sim$ 27 K. This is similar to measurements in both overdoped La_2CuO_{4+y}, where a levelling off of the dynamic incommensurate spin response has been reported below $T_C\sim$ 42 K (Lee et al., 1999) and also in $La_{2-x}Ba_xCuO_4$ (x=0.125) in the normal state (Fujita et al., 2004). In the latter compound, as a function of frequency there is relatively little change in $\chi''(\omega)$ at low temperature (8 K), whereas it drops rapidly in the present x=0.095 sample. As the temperature is raised, $\chi''(\omega)$ varies linearly with frequency at lower energy transfers below 10 meV in the x=0.125 sample for T> 65 K, whereas it declines with increasing ω in x=0.095 for all T< 60 K. These low energy excitations have some of the characteristics of the spin waves observed in the parent compound La_2CuO_4 (Yamada et al., 1989) as one warms through the Néel temperature, where instantaneous spin correlations with the character of the Néel state persist into the paramagnetic regime (Shirane et al., 1987).

The form of $\chi''(\omega)$ varies dramatically as a function of doping in the related $La_{2-x}Sr_xCuO_4$ compounds. In the optimally and slightly overdoped $La_{2-x}Sr_xCuO_4$ samples (x=0.15,0.18) (Yamada et al., 1995, 1997), there is a characteristic energy of $\sim$ 7 meV below which the dynamic susceptibility is dramatically reduced in the superconducting state - the opening up of a spin gap. However, on the underdoped side of the superconducting dome there

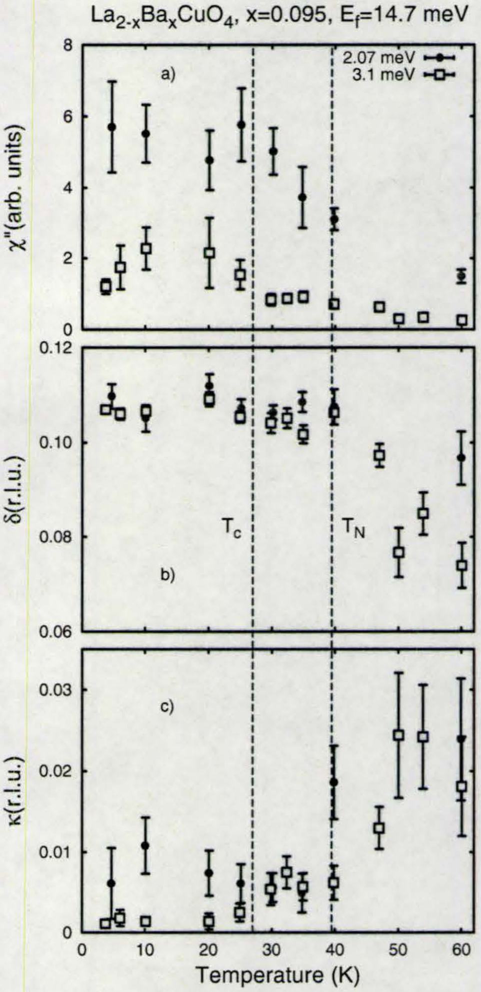

Figure 5.8: The temperature dependence of the parameters extracted from fitting the low energy inelastic magnetic scattering. We show a) χ"(Q, ω=2.07 and 3.1 meV); b) the incommensurability δ; and c) the inverse correlation length κ. The dashed lines indicate the superconducting (T_C= 27 K) and magnetic (T_N=39.5 ±0.3 K) transition temperatures.

is finite spectral weight in the spin response at all low energy transfers (Lee et al., 2000; Hiraka et al., 2001).

The magnetic properties of the $YBa_2Cu_3O_{6+x}$ family show significant differences from the $La_{2-x}Sr_xCuO_4$ and $La_{2-x}Ba_xCuO_4$ systems such as the absence of incommensurate elastic Bragg scattering. Still, the $YBa_2Cu_3O_{6+x}$ system is well studied and a comparison can be made to our measured low energy dynamic susceptibility in $La_{2-x}Ba_xCuO_4$ (x=0.095). Recent neutron scattering measurements (Stock et al., 2006) on $YBa_2Cu_3O_{6.5}$ with T_C=59 K ($x_{eff} \sim 0.06$ for comparison to $La_{2-x}Sr_xCuO_4$ and $La_{2-x}Ba_xCuO_4$) also show a suppression of the dynamic susceptibility at the commensurate (0.5, 0.5, 0) position below $\sim$ 15 meV. Measurements on very underdoped $YBa_2Cu_3O_{6.35}$ (Stock et al., 2007) with T_C=18 K show a cone of spin excitations out of the commensurate (0.5, 0.5) position in reciprocal space similar to that observed in insulating $YBa_2Cu_3O_{6.15}$ (Shamoto et al., 1993).

Figure 5.8 b) and c) show that the incommensurate wave-vector, δ and the inverse correlation length, κ, correlate most strongly with the disappearance of the static spin order near $T_N \sim 39$ K, which is not surprising. Above T_N the increase in κ may indicate that stripe correlations are weakened by thermal fluctuations that broaden the hole distribution about antiphase domain boundaries. As described in detail in Ref. (Savici et al., 2007) and references therein, the appropriate functional from to describe the scattering may depend on the dimensionality of the system, as well as disorder. However, using a Lorentzian form allows direct comparison with related compounds (Fujita et al., 2002c, 2004). Analysis using a Lorentzian function raised to the power 3/2 gave qualitatively similar results. Such a form has been observed in two dimensional random field Ising model systems.

5.3 Neutron scattering from $La_{2-x}Ba_xCuO_4$ in the spin glass regime

Neutron scattering measurements on $La_{2-x}Ba_xCuO_4$single crystals with relatively low doping, x=0.05 and 0.025, were carried on the DCS spectrometer at NIST and the 4F1 triple axis spectrometer at LLB, both on a cold neutron source. We chose cold neutron source instruments in order to utilize longer wavelength neutrons which were anticipated to be helpful in resolving the low incommensurate wave-vector, δ, expected for lower Ba concentrations. Definitive measurements of the incommensurate spin structure are progressively more difficult at lower doping, as the incommensurability δ is proportional to the doping level x (Yamada et al., 1998). In order to directly compare with superconducting samples, our $La_{2-x}Ba_xCuO_4$ x=0.08 sample was also measured with the DCS spectrometer. All measurements are performed with the samples aligned with the $(h, k, 0)$ basal plane coincident with horizontal scattering plane. Detailed DCS and triple-axis spectrometer configurations are listed in Table 3.1 and 3.2

5.3.1 Elastic neutron scattering studies using the DCS spectrometer

We first discuss our results obtained using DCS measurement. As described in Chapter 3, the DCS spectrometer can easily explore a broad range of Q space, which is well suited to searching for incommensurate magnetic Bragg peaks. Reciprocal space maps collected by DCS spectrometer at T~ 1.5 K are shown in figure 5.9, where in all cases we have integrated over the elastic scattering between -0.1 meV $\leq \hbar\omega \leq$ 0.1 meV.

We start with the x=0.08 sample to confirm our thermal triple-axis experiment results discussed early in this chapter. As shown in figure 5.9 c), magnetic Bragg peaks occur at (0.5$\pm\delta$,0.5,0) and (0.5, 0.5$\pm\delta$, 0) with δ = 0.107(3), measured using λ=4.8 Å incident neutrons with an energy resolution of 118.2μeV FWHM. This indicates static collinear incommensurate spin order, with ordering wavevectors parallel to a^*_{tetra}. A single (1, -1, 0) structural Bragg peak is evident in figure 5.9 c), indicating the x=0.08 sample is in its LTT phase at 1.5 K. These results agree with our thermal neutron triple-axis measurement results (Dunsiger et al., 2008a).

Figure 5.9 a) shows the elastic reciprocal space map centered on (0.5, 0.5, 0) from the lightly doped $La_{2-x}Ba_xCuO_4$ (x=0.025) compound, using λ=6.2Å incident neutrons with energy resolution 58.4μeV FWHM. Additional measurements were taken with both 6.2 Å and 8 Å incident neutrons, in two different Brillouin zones, centered on both (0.5, 0.5, 0) and (0.5, -0.5, 0), which gave consistent results (not shown here). Unlike the collinear magnetic peaks observed in the x=0.08 sample, a remarkable isolated pair of diagonal incommensurate magnetic Bragg peaks are evident near (0.5-$\delta/\sqrt{2}$, 0.5+$\delta/\sqrt{2}$, 0) with an incommensurability δ=0.017(1), in tetragonal notation. This is clear evidence for a static, one dimensional, diagonal incommensurate spin modulation along b_{ortho}, which rotate 45° respect to b_{tetr}. Nuclear Bragg peaks associated with four MTO twin domains in the x=0.025 sample are visible near (1, 1, 0) (λ=4.8 Å) are shown in the Figure 5.9 as well. The integrated intensity of the majority twin peak is $\sim$ 4 times larger than the minority peaks. This accounts for the single pair of incommensurate magnetic Bragg peaks: the magnetic scattering from this x=0.025 sample closely resembles that from a

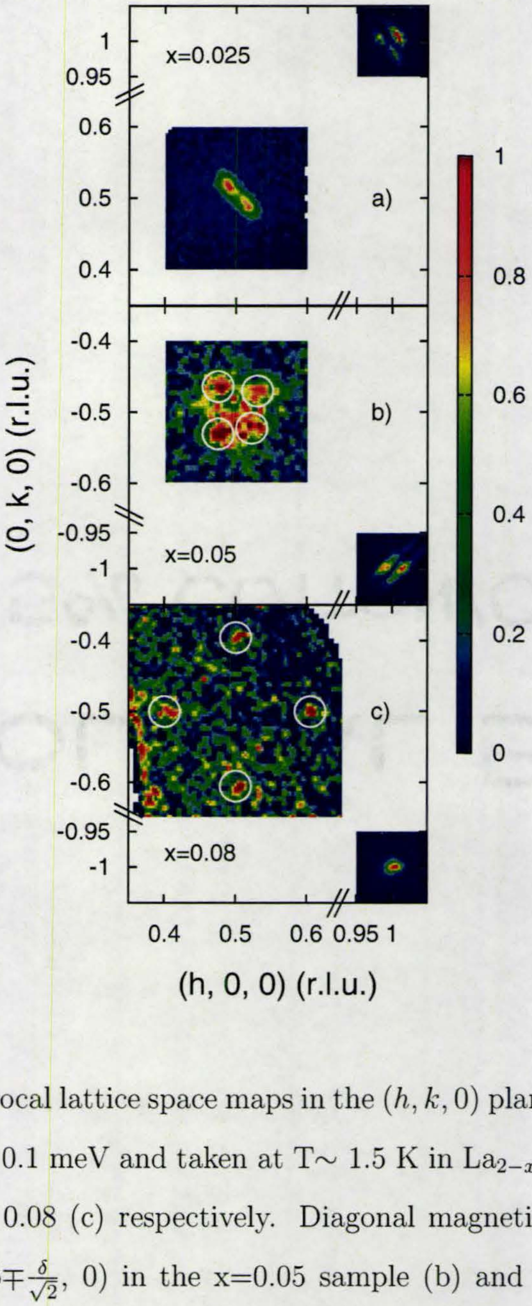

Figure 5.9: Reciprocal lattice space maps in the $(h, k, 0)$ plane, integrating over -0.1 meV $\leq \hbar\omega \leq$ 0.1 meV and taken at T$\sim$ 1.5 K in $La_{2-x}Ba_xCuO_4$ x=0.025 (a), 0.05 (b) and 0.08 (c) respectively. Diagonal magnetic Bragg scattering near $(0.5\pm\frac{\delta}{\sqrt{2}}, 0.5\mp\frac{\delta}{\sqrt{2}}, 0)$ in the x=0.05 sample (b) and collinear magnetic Bragg scattering near (0.5$\pm\delta$,0.5,0) and (0.5,0.5$\pm\delta$,0) in the x=0.08 sample (c) have been circled for clarity.

de-twinned MTO structure with a unique b-direction.

The same type of reciprocal space map is shown in figure 5.9 b) for the x=0.05 sample, again using with λ=4.8 Å incident neutrons. Two nuclear Bragg peaks are now clear, centred around the tetragonal (1, -1, 0) position, associated with two out of four possible twin domains in the sample of $La_{2-x}Ba_xCuO_4$ (x=0.05) at T=1.5 K in its MTO phase. The relative intensities of the two (1, -1, 0) peaks indicate the two twin domains have comparable volume fractions. Magnetic Bragg peaks arising from static incommensurate spin order are again observed along the diagonal directions, that is along each of the b_{ortho} axes. One pair of magnetic Bragg peaks is associated with each twin domain, such that a one dimensional spin modulation occurs only along the orthorhombic b axis, as clearly illustrated in Ref (Wakimoto et al., 2000).

Such diagonal stripes have been predicted theoretically (Poilblanc and Rice, 1989; Zaanen and Gunnarsson, 1989) and have also been observed in insulating $La_{2-2x}Sr_xNiO_4$ (Tranquada et al., 1996; Yoshizawa et al., 2000). The pattern is very similar to that observed in underdoped $La_{2-x}Sr_xCuO_4$ ($0.02 \leq x \leq 0.055$) (Wakimoto et al., 1999; Matsuda et al., 2000; Wakimoto et al., 2000), where the diagonal spin modulation is also along the orthorhombic b axis and is considered to be an intrinsic property of the entire insulating spin glass region, in contrast to the parallel spin modulation observed in the superconducting phase of $La_{2-x}Sr_xCuO_4$.

5.3.2 Elastic neutron scattering studies of $La_{2-x}Ba_xCuO_4$ with x=0.05 using the 4F1 triple-axis spectrometer

Complementary cold triple axis neutron scattering experiments were undertaken on the same $La_{2-x}Ba_xCuO_4$ (x=0.05) single crystal using the 4F1 spectrometer at the LLB. The (002) reflection of pyrolytic graphite was used for both monochromator and flat analyzer (E_i=E_f=5 meV). We employed $open - 60' - 60' - open$ collimation along the beam path from source through sample to detector, yielding an energy resolution of 105 μeV with elastic scattering. Cooled Be filters were placed in both the incident and scattered beams to remove contamination from higher order neutrons. The spectrometer was aligned to concentrate on a single twin domain with orthorhombic coordinate unit cell with $a_{ortho} = 5.3380$Å, $b_{ortho} = 5.4125$Å. Representative elastic scans along the orthorhombic and tetragonal b* axes are shown in figure 5.10 a) and b) respectively, and has been converted with tetragonal notation where $a_{tetr} = a_{ortho}/\sqrt{2} \simeq 3.78\mathring{A}$. Well resolved elastic magnetic peaks are clearly visible in figure 5.10 a), corresponding to the static spin modulation along the orthorhombic b^*_{ortho} direction. By contrast, the intensity centred on the commensurate position in figure 5.10 b) is due to the tails of the incommensurate peaks. There is no evidence of any coexistence of diagonal and collinear spin ordering and this result agree with our DCS measurement. Elastic scans along either directions at 28 K show flat background (see figure 5.10) indicating no higher order contamination neutrons collected at (0.5, 0.5, 0) position.

Quantitatively, the data in figure 5.10 a) have been analysed using a resolution convolution of four, one dimensional Lorentzian functions similar to

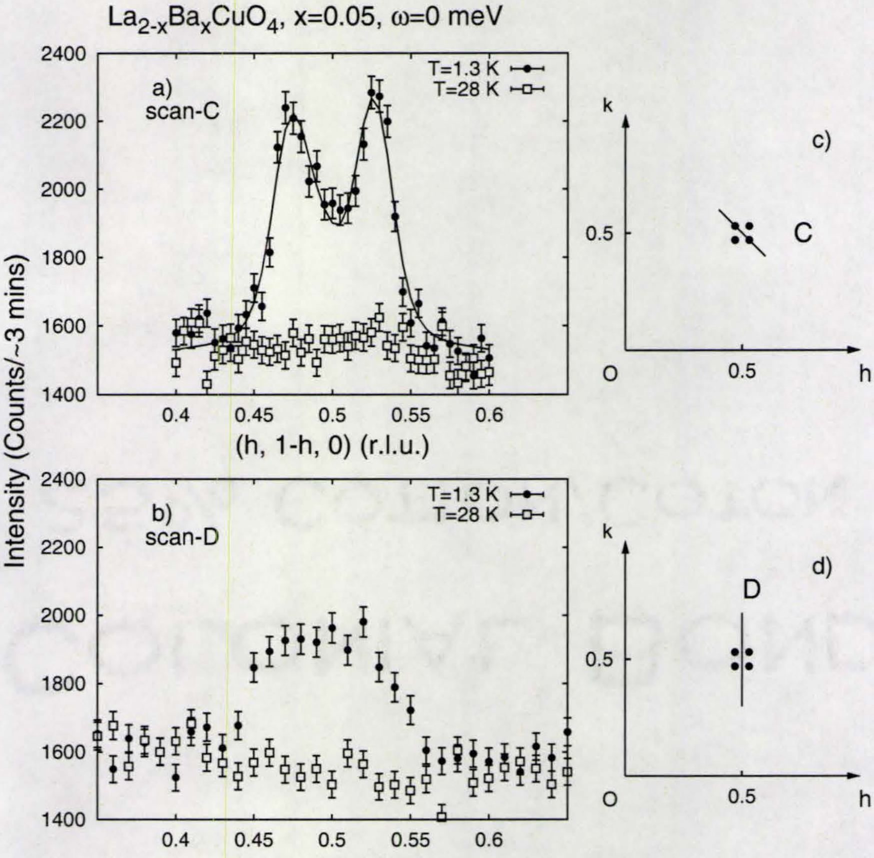

Figure 5.10: Static incommensurate magnetic peaks with δ=0.039 in $La_{1.95}Ba_{0.05}CuO_4$ at T=1.5 K, along a) the orthorhombic'diagonal' direction, scan-C, b) the 'collinear' direction, scan-D. The solid line is fitting results described in the text. The circles in c) and d) schematically show the positions of the four diagonal, incommensurate peaks

superconductor samples (Equ. 5.1)

$$S(Q) = \frac{A}{\pi} \sum_{n=1}^{4} \frac{\kappa}{(Q - Q_{\delta,n})^2 + \kappa^2} \tag{5.4}$$

to extract values for the incommensurate wavevector δ and inverse correlation length κ. $Q_{\delta,n}$ represents the four incommensurate wave vectors at $(1, \pm\sqrt{2}\delta, 0)_{ortho}$ and $(0.987 \pm \sqrt{2}\delta \cos\theta, 0.0075 \pm \sqrt{2}\delta \sin\theta, 0)_{ortho}$. The latter contribution arises from the the wings of the second domain, characterised by a nuclear Bragg peak centered at $(1.974, 0.015, 0)_{ortho}$, such that $\tan\theta = 0.015/1.974$. This functional form assumes the magnetic scattering consists of rods running along the c* axis as used before. The magnetic peaks are relatively sharp and practically resolution limited, with an incommensurability δ=0.0389(6) r.l.u. in tetragonal notation and a HWHM κ=0.0063(16) Å^{-1}, equivalent to a correlation length of 159(50) Å within the basal plane. This is of a comparable magnitude as that observed in the superconducting state of $La_{2-x}Ba_xCuO_4$ (x=0.095, 0.08) as discussed before (Dunsiger et al., 2008a). However, it should be noted that the values quoted for the related $La_{2-x}Sr_xCuO_4$ x=0.05 compound are much shorter (Wakimoto et al., 2000; Bao et al., 2007), between 25 - 35 Å.

The temperature dependence of the incommensurate magnetic elastic scattering is shown in figure 5.11 for the x=0.05 and 0.025 samples, which display the diagonal incommensurate spin structures. Triple axis measurements of the magnetic Bragg intensity at (0.526, 0.474, 0) in the x=0.05 sample may be compared with DCS measurements of the intensity integrated between $-0.1 \leq \hbar\omega \leq 0.1$ meV, as the energy resolution is similar.

Figure 5.11 shows the decrease of the static incommensurate magnetic Bragg intensity in the x=0.05 sample on warming to T=10 K, consistent with

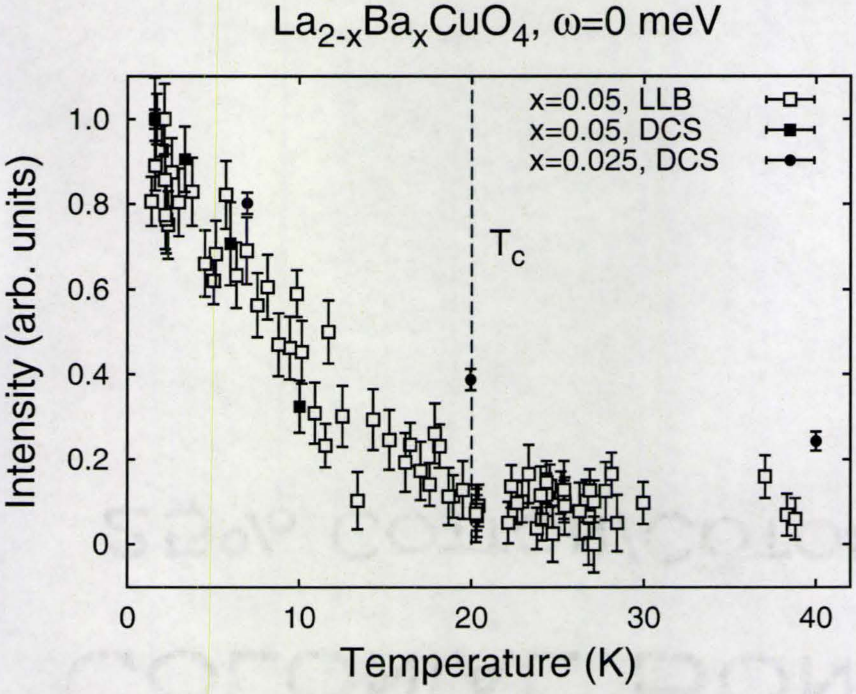

Figure 5.11: The temperature dependence of the net elastic incommensurate magnetic scattering in $La_{2-x}Ba_xCuO_4$, x=0.05, measured at (0.526, 0.474, 0), using triple axis (open squares) and DCS (filled squares) neutron diffraction techniques. Integrated intensity between $-0.1 \leq \hbar\omega \leq 0.1$ meV as a function of temperature in $La_{2-x}Ba_xCuO_4$ (x=0.025) measured using the DCS spectrometer (filled circles). The intensity has been normalized by the maximum intensity at lowest collecting temperature.

the temperature dependence of the break between the FC and ZFC susceptibilities shown in figure 2.3 c). For temperatures beyond 10 K, a continued weak fall off of the intensity with increasing temperature is observed to ~ 25 K, beyond which no vestiges of the static signal are easily observable. Our data for the temperature dependence of the incommensurate magnetic scattering in the x=0.025 sample is less extensive, but qualitatively similar to that of the x=0.05 sample, as may be expected due to the similarity in the temperature dependence of their ZFC vs FC susceptibilities and therefore their spin glass ground states.

5.4 Incommensurability as a function of doping in $La_{2-x}Ba_xCuO_4$

It is also interesting to examine the correlation between Ba-content, x, and incommensurability, δ, in $La_{2-x}Ba_xCuO_4$ and compare these relationships to those reported for $La_{2-x}Sr_xCuO_4$. Figure 5.12 shows the incommensurability δ vs Ba-content, x and we compare our results with those of several underdoped $La_{2-x}Sr_xCuO_4$ samples at Sr concentrations. Data from x=0.125 sample of $La_{2-x}Ba_xCuO_4$(Fujita et al., 2004) and some preliminary measurement results with x=0.0125 and 0.035 samples are also included.

Despite differences at higher doping levels, the overall δ vs x behavior is very similar in this range of underdoped $La_{2-x}Ba_xCuO_4$ and $La_{2-x}Sr_xCuO_4$. The same transition, from diagonal to collinear incommensurate spin ordering is roughly coincident with the transition from an insulating spin glass ground state to a superconducting ground state near $x_C \sim 0.055$ for both

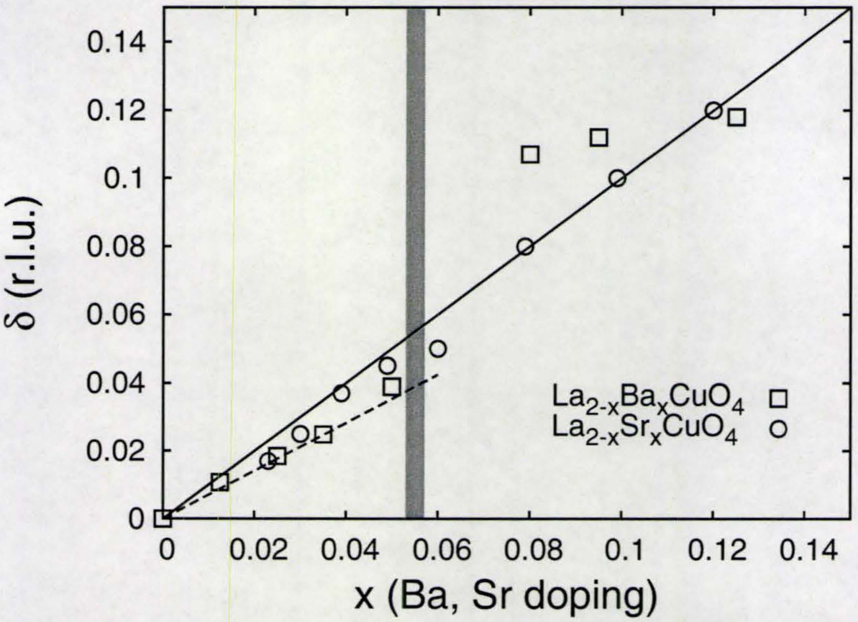

Figure 5.12: Incommensurability, δ vs Ba/Sr concentration, x, plotted using the current results and those from the literature, as described in the text. The transition from diagonal to collinear incommensuration in the $\mathrm{La}_{2-x}\mathrm{Sr}_x\mathrm{CuO}_4$ system near x=0.055 (Matsuda et al., 2000) is shown as the shaded vertical line.

$La_{2-x}Ba_xCuO_4$ and $La_{2-x}Sr_xCuO_4$ families, as shown by the vertical line in figure 5.12. The complex low temperature structural phase diagram of $La_{2-x}Ba_xCuO_4$ with LTT phase and near-complete suppression of superconductivity near x=0.125, clearly does not interfere with the rotation of the incommensurate spin ordering as a function of doping.

For superconducting samples with x>0.055, the incommensurate spin ordering is consistent with a picture of collinear (as opposed to diagonal) incommensurate spin ordering. In this Sr-content regime, δ tracks x well, assuming stoichiometric oxygen content (Yamada et al., 1998; Kimura et al., 1999; Matsuda et al., 2000; Wakimoto et al., 2000). At higher doping levels the incommensurate wave-vector δ in the x=0.08 and x=0.095 $La_{2-x}Ba_xCuO_4$ samples shows relatively little x-dependence. Indeed, we observe δ values which are only ~ 9 % less than that displayed by x=0.125 $La_{2-x}Ba_xCuO_4$, thereby departing significantly from the approximately linear δ vs x relation characterizing the underdoped $La_{2-x}Sr_xCuO_4$ studies.

It is possible that this difference between underdoped $La_{2-x}Ba_xCuO_4$ and $La_{2-x}Sr_xCuO_4$ also arises due to the MTO-LTT structural phase transition, occurring in $La_{2-x}Ba_xCuO_4$ but absent in $La_{2-x}Sr_xCuO_4$. It is also conceivable that it arises due to some small oxygen off-stoichiometry, such that our samples have the composition $La_{2-x}Ba_xCuO_{4+y}$, with oxygen stoichiometry greater than 4. Such excess oxygen would give rise to an effective hole doping given by x_{eff} = x+2y. To bring the δ values for x=0.08 and 0.095 back onto the linear relationship between δ and x_{eff} seen in $La_{2-x}Sr_xCuO_4$, small, but positive values of y: 0.013 and 0.0075 for the x=0.08 and x=0.095 $La_{2-x}Ba_xCuO_{4+y}$ samples respectively would be required. This is too small to be detectable and runs counter to what is concluded in $La_{2-x}Sr_xCuO_{4+y}$. In underdoped $La_{2-x}Sr_xCuO_{4+y}$, the superconducting T_c is maximized by annealing in oxygen, at which point the measured δ vs Sr concentration, x, lie on the straight line (Yamada et al., 1998). Consequently, as grown $La_{2-x}Sr_xCuO_{4+y}$ tends to be oxygen deficient (y<0) and annealing in oxygen results in stoichiometric $La_{2-x}Sr_xCuO_4$. This is also expected to be true for underdoped $La_{2-x}Ba_xCuO_{4+y}$, which would imply that the deviation of δ vs x from a linear relationship is intrinsic to stoichiometric $La_{2-x}Ba_xCuO_4$, a surprising result.

For lower doped $La_{2-x}Ba_xCuO_4$ with x<0.055, the incommensurate wave-vector δ agrees suprisingly well with the straight line relation $\delta = x/\sqrt{2}$. The factor of $\sqrt{2}$ comes from the diagonal modulation, where d-spacing along (1, 1, 0) direction is approximately $\sqrt{2}$ times d-spacing along (1, 0, 0) or (0, 1, 0) direction. These results in lightly doped $La_{2-x}Ba_xCuO_4$ samples also confirm we obtain the right order of Ba doping levels in this regime.

5.5 Discussion

We have observed the static incommensurate spin order in all four $La_{2-x}Ba_xCuO_4$ single crystal samples. In high T_c superconductor samples, x=0.095 and 0.08, static spin order is arranged along the collinear direction and coexists with superconductivity at low temperatures. In lower doping samples, x=0.05 and 0.025, static spin order appears along diagonal direction. The superconducting and magnetic phase transition temperature as well as incommensurate wave-vector δ for each sample are listed in Table 5.1.

One significant finding of this study is the field independence of the incommensurate magnetic order in the x=0.095 sample, in contrast to what has been reported for other superconducting La-214 cuprates. Studies of the spin

Table 5.1: Summary of superconducting (T_C), magnetic (T_N) phase transition temperatures and incommensurate wave-vector δ

x	T_c(K)	T_N(K)	δ(r.l.u.)$_{tetr}$
0.125[1]	~4	50	0.118
0.095	27	39.5	0.112
0.08	29	~39	0.107
0.05	~20	~25	0.035
0.025		>40	0.0125

[1] From Ref. (Fujita et al., 2004)

ordering as a function of magnetic field in other superconducting systems with large magnetic volume fractions should prove illuminating. In addition, the x-dependence to the incommensurability appears to be substantially weaker than that seen in $La_{2-x}Sr_xCuO_4$, where a linear relationship is observed over this range of concentration.

Another interesting results is the single pair incommensurate spin order observed in x=0.025 sample. While Bragg peak (1, 1, 0) indicates the sample with possesses a twin structure, however, magnetic scattering show single magnetic ordering domain present at low temperatures. Even though minor difference are evident, these results are in broad agreement with the evolution of incommensurate spin order in other well studied high temperature La-214 cuprate superconductors, such as $La_{2-x}Sr_xCuO_4$ or La_2CuO_{4+y}, implying that the phenomenon is a generic feature of the underdoped La-214 cuprates.

Chapter 6

Conclusion

After being discovered over 20 years ago, high T_c cuprates are remain one of the most important challenges in condensed matter physics. Most surprisingly, the original "Zurich material" high temperature superconductor, $La_{2-x}Ba_xCuO_4$, has not been extensively studied due to the relative difficulty of obtaining high quality single crystals until recently (Fujita et al., 2004; Tranquada et al., 2004). In this thesis, we reported the successful growth of large, high quality $La_{2-x}Ba_xCuO_4$ single crystals with series of doping levels by using TSFZ techniques. Being one of the few teams who can grow high quality $La_{2-x}Ba_xCuO_4$ single crystals gives us great advantage, as the crystals allow us to carry on comprehensive neutron and X-ray scattering studies on the original family of high temperature superconductors.

By using high resolution X-ray scattering studies on $La_{2-x}Ba_xCuO_4$ at relatively high doping (x=0.0125, 0.095 and 0.08), we identify three existing structural phases (HTT, MTO and LTT) with two phase transition temperatures, T_{d1} and T_{d2}. After carefully analyzing the critical orthorhombic strain near the continuously HTT→ MTO phase boundary, we obtain a common critical exponent $\beta = 0.34 \pm 0.04$, which is consistent with 3DXY universality expected from relevant theory. Neutron scattering experiments were carried out on all $La_{2-x}Ba_xCuO_4$ samples we produced using either triple-axis or time-of-flight methods. Some samples were measured using both neutron scattering techniques. We observed incommensurate spin ordering developing in all $La_{2-x}Ba_xCuO_4$ samples at low temperature. Our neutron scattering experiment results on $La_{2-x}Ba_xCuO_4$ single crystals could be compared to results on the much more extensively studied $La_{2-x}Sr_xCuO_4$ system. In both cases, incommensurate spin order transforms from being aligned along the diagonal direction to along the collinear direction around a critical doping x$\sim$0.055, which is approximately coincident with the transition from the insulating spin glass to the superconducting state. Despite some minor differences at higher doping levels, the overall incommensurability δ vs. the doping level x behaviour in our $La_{2-x}Ba_xCuO_4$ single crystal samples is also similar to the results that has been reported in the $La_{2-x}Sr_xCuO_4$ system. In addition, by examining the calculated orthorhombic strain, Δ, as the function of the doping levels, x, we found another scale to calibrate the Ba concentration in our $La_{2-x}Ba_xCuO_4$ single crystal samples. This scale is particularly useful for the low doped (x$\lesssim$0.5) $La_{2-x}Ba_xCuO_4$ single crystals due to the absence of T_{d2} and T_c in such a low doping range.

Our neutron scattering results on $La_{2-x}Ba_xCuO_4$ single crystal samples show several important differences relative to results on $La_{2-x}Sr_xCuO_4$. One unexpected result is the magnetic field independent incommensurate magnetism in the superconducting sample of $La_{2-x}Ba_xCuO_4$ with x=0.095, in contrast to other superconducting La-214 cuprates. Another interesting result is the observation of a single pair of diagonal incommensurate magnetic

Bragg peaks in the lowest doping sample (x=0.025). Although the sample is orthorhombic and twinned, only two incommensurate magnetic peaks are detected along the diagonal direction instead of the expected four peaks, suggesting an intrinsic "one dimension" incommensurate magnetic structure in lightly doped $La_{2-x}Ba_xCuO_4$ materials.

In this thesis, we have studied and discussed the structural and magnetic properties of high quality $La_{2-x}Ba_xCuO_4$ single crystals as the function of doping. Compared with the literature on $La_{2-x}Sr_xCuO_4$ single crystals, the experimental results on $La_{2-x}Ba_xCuO_4$ remain limited especially for neutron scattering data on large single $La_{2-x}Ba_xCuO_4$ crystals. With the availability of high quality $La_{2-x}Ba_xCuO_4$ single crystals, further extensive studies can be carried out which should fully elucidate the evolution of magnetism and superconductivity as the function of doping in the $La_{2-x}Ba_xCuO_4$ system.

Bibliography

J. G. Bednorz and K. A. Müller, Zeitschrift für Physik B Condensed Matter **64**, 189 (1986).

M. A. Kastner, R. J. Birgeneau, G. Shirane, and Y. Endoh, Rev. Mod. Phys. **70**, 897 (1998).

R. J. Birgeneau, C. Stock, J. M. Tranquada, and K. Yamada, Journal of the Physical Society of Japan **75**, 111003 (2006).

M. Eschrig, Advances in Physics **55**, 47 (2006).

H. F. Fong, P. Bourges, Y. Sidis, L. P. Regnault, A. Ivanov, G. D. Gu, N. Koshizuka, and B. Keimer, Nature **398**, 588 (1999).

J. P. Castellan, B. D. Gaulin, H. A. Dabkowska, A. Nabialek, G. Gu, X. Liu, and Z. Islam, Physical Review B **73**, 174505 (2006).

Y. Zhao, B. D. Gaulin, J. P. Castellan, J. P. C. Ruff, S. R. Dunsiger, G. D. Gu, and H. A. Dabkowska, Physical Review B (Condensed Matter and Materials Physics) **76**, 184121 (2007).

S. R. Dunsiger, Y. Zhao, Z. Yamani, W. J. L. Buyers, H. A. Dabkowska, and

B. D. Gaulin, Physical Review B (Condensed Matter and Materials Physics) **77**, 224410 (2008a).

S. R. Dunsiger, Y. Zhao, B. D. Gaulin, Y. Qiu, P. Bourges, Y. Sidis, J. R. D. Copley, A. Kallin, E. M. Mazurek, and H. A. Dabkowska, Physical Review B (Condensed Matter and Materials Physics) **78**, 092507 (2008b).

T. Adachi, T. Noji, and Y. Koike, Phys. Rev. B **64**, 144524 (2001).

J. D. Axe, D. E. Cox, K. Mohanty, H. Moudden, A. R. Moodenbaugh, Y. Xu, and T. R. Thurston, IBM Journal of Research and Development **33**, 382 (1989a).

J. D. Axe, A. H. Moudden, D. Hohlwein, D. E. Cox, K. M. Mohanty, A. R. Moodenbaugh, and Y. Xu, Phys. Rev. Lett. **62**, 2751 (1989b).

T. Suzuki and T. Fujita, Physica C: Superconductivity **159**, 111 (1989a).

T. Suzuki and T. Fujita, Journal of the Physical Society of Japan **58**, 1883 (1989b).

A. R. Moodenbaugh, Y. Xu, M. Suenaga, T. J. Folkerts, and R. N. Shelton, Phys. Rev. B **38**, 4596 (1988).

T. Nagano, Y. Tomioka, Y. Nakayama, K. Kishio, and K. Kitazawa, Phys. Rev. B **48**, 9689 (1993).

P. G. Radaelli, D. G. Hinks, A. W. Mitchell, B. A. Hunter, J. L. Wagner, B. Dabrowski, K. G. Vandervoort, H. K. Viswanathan, and J. D. Jorgensen, Phys. Rev. B **49**, 4163 (1994).

M. Fujita, H. Goka, K. Yamada, J. M. Tranquada, and L. P. Regnault, Phys.Rev.B **70**, 104517 (2004).

J. M. Tranquada, H. Woo, T. G. Perring, H. Goka, G. D. Gu, G. Xu, M. Fujita, and K. Yamada, Nature **429**, 534 (2004).

R. J. Birgeneau, C. Y. Chen, D. R. Gabbe, H. P. Jenssen, M. A. Kastner, C. J. Peters, P. J. Picone, T. Thio, T. R. Thurston, H. L. Tuller, et al., Phys. Rev. Lett. **59**, 1329 (1987).

D. Vaknin, S. K. Sinha, D. E. Moncton, D. C. Johnston, J. M. Newsam, C. R. Safinya, and H. E. King, Phys. Rev. Lett. **58**, 2802 (1987).

P. Böni, J. D. Axe, G. Shirane, R. J. Birgeneau, D. R. Gabbe, H. P. Jenssen, M. A. Kastner, C. J. Peters, P. J. Picone, and T. R. Thurston, Phys.Rev.B **38**, 185 (1988).

M. Braden, W. Schnelle, W. Schwarz, N. Pyka, G. Heger, Z. Fisk, K. Gamayunov, I. Tanaka, and H. Kojima, Zeitschrift für Physik B Condensed Matter **V94**, 29 (1994).

W. Ting and K. Fossheim, Phys. Rev. B **48**, 16751 (1993).

T. R. Thurston, R. J. Birgeneau, D. R. Gabbe, H. P. Jenssen, M. A. Kastner, P. J. Picone, N. W. Preyer, J. D. Axe, P. Böni, G. Shirane, et al., Phys. Rev. B **39**, 4327 (1989).

M. F. Collins, *Magnetic Critical Scattering*, Oxford series on neutron scattering in condensed matter (Oxford University Press, 1989).

S. A. Kivelson, I. P. Bindloss, E. Fradkin, V. Oganesyan, J. M. Tranquada, A. Kapitulnik, and C. Howald, Reviews of Modern Physics **75**, 1201 (2003).

M. Matsuda, M. Fujita, K. Yamada, R. J. Birgeneau, M. A. Kastner, H. Hiraka, Y. Endoh, S. Wakimoto, and G. Shirane, Phys. Rev. B **62**, 9148 (2000).

S. Wakimoto, R. J. Birgeneau, M. A. Kastner, Y. S. Lee, R. Erwin, P. M. Gehring, S. H. Lee, M. Fujita, K. Yamada, Y. Endoh, et al., Phys. Rev. B **61**, 3699 (2000).

H. Kimura, K. Hirota, H. Matsushita, K. Yamada, Y. Endoh, S.-H. Lee, C. F. Majkrzak, R. Erwin, G. Shirane, M. Greven, et al., Phys. Rev. B **59**, 6517 (1999).

S. Wakimoto, H. Zhang, K. Yamada, I. Swainson, H. Kim, and R. J. Birgeneau, Physical Review Letters **92**, 217004 (2004).

E. Fawcett, Rev. Mod. Phys. **60**, 209 (1988).

M. R. Norman and C. Pépin, Reports on Progress in Physics **66**, 1547 (2003).

W. H. Zachariasen, *Theory of X-ray diffraction in crystals* (Dover publications Inc., New York, 1945).

G. L. Squires, *Introduction to the theory of thermal neutron scattering* (Cambridge University Press, New York, 1978).

M. J. Cooper and R. Nathans, Acta Crystallographica **23**, 357 (1967).

R. B. Rogge, Ph.D. thesis, McMaster University (1994).

Y. Zhu, A. R. Moodenbaugh, Z. X. Cai, J. Tafto, M. Suenaga, and D. O. Welch, Phys. Rev. Lett. **73**, 3026 (1994).

M. Fujita, H. Goka, K. Yamada, and M. Matsuda, Phys. Rev. Lett. **88**, 167008 (2002a).

J. C. Le Guillou and J. Zinn-Justin, Phys. Rev. Lett. **39**, 95 (1977).

J. C. Le Guillou and J. Zinn-Justin, Phys. Rev. B **21**, 3976 (1980).

M. Fujita, K. Yamada, H. Hiraka, P. M. Gehring, S. H. Lee, S. Wakimoto, and G. Shirane, Phys. Rev. B **65**, 064505 (2002b).

B. Lake, H. M. Ronnow, N. B. Christensen, G. Aeppli, K. Lefmann, D. F. McMorrow, P. Vorderwisch, P. Smeibidl, N. Mangkorntong, T. Sasagawa, et al., Nature **415**, 299 (2002).

S. Katano, M. Sato, K. Yamada, T. Suzuki, and T. Fukase, Phys. Rev. B **62**, R14677 (2000).

B. Lake, K. Lefmann, N. B. Christensen, G. Aeppli, D. F. McMorrow, H. M. Ronnow, P. Vorderwisch, P. Smeibidl, N. Mangkorntong, T. Sasagawa, et al., Nature Materials **4**, 658 (2005).

B. Lake, G. Aeppli, K. N. Clausen, D. F. McMorrow, K. Lefmann, N. E. Hussey, N. Mangkorntong, M. Nohara, H. Takagi, T. E. Mason, et al., Science **291**, 1759 (2001), URL `10.1126/science.1056986; http://www.sciencemag.org/cgi/content/abstract/291/5509/1759`.

B. Khaykovich, S. Wakimoto, R. J. Birgeneau, M. A. Kastner, Y. S. Lee, P. Smeibidl, P. Vorderwisch, and K. Yamada, Physical Review B (Condensed Matter and Materials Physics) **71**, 220508 (2005).

E. Demler, S. Sachdev, and Y. Zhang, Phys. Rev. Lett. **87**, 067202 (2001).

H. Takagi, S.-i. Uchida, H. Obara, K. Kishio, K. Kitazawa, K. Fueki, and S. Tanaka, Jpn. J. Appl. Phys. **26**, L434 (1987).

G. S. Boebinger, Y. Ando, A. Passner, T. Kimura, M. Okuya, J. Shimoyama, K. Kishio, K. Tamasaku, N. Ichikawa, and S. Uchida, Phys. Rev. Lett. **77**, 5417 (1996).

B. Khaykovich, Y. S. Lee, R. W. Erwin, S.-H. Lee, S. Wakimoto, K. J. Thomas, M. A. Kastner, and R. J. Birgeneau, Phys. Rev. B **66**, 014528 (2002).

A. T. Savici, Y. Fudamoto, I. M. Gat, T. Ito, M. I. Larkin, Y. J. Uemura, G. M. Luke, K. M. Kojima, Y. S. Lee, M. A. Kastner, et al., Phys. Rev. B **66**, 014524 (2002).

Y. S. Lee, R. J. Birgeneau, M. A. Kastner, Y. Endoh, S. Wakimoto, K. Yamada, R. W. Erwin, S.-H. Lee, and G. Shirane, Phys. Rev. B **60**, 3643 (1999).

K. Yamada, K. Kakurai, Y. Endoh, T. R. Thurston, M. A. Kastner, R. J. Birgeneau, G. Shirane, Y. Hidaka, and T. Murakami, Phys. Rev. B **40**, 4557 (1989).

G. Shirane, Y. Endoh, R. J. Birgeneau, M. A. Kastner, Y. Hidaka, M. Oda, M. Suzuki, and T. Murakami, Phys. Rev. Lett. **59**, 1613 (1987).

K. Yamada, S. Wakimoto, G. Shirane, C. H. Lee, M. A. Kastner, S. Hosoya, M. Greven, Y. Endoh, and R. J. Birgeneau, Phys. Rev. Lett. **75**, 1626 (1995).

K. Yamada, C. H. Lee, Y. Endoh, G. Shirane, R. J. Birgeneau, and M. A. Kastner, Physica C: Superconductivity **282-287**, 85 (1997).

C.-H. Lee, K. Yamada, Y. Endoh, G. Shirane, R. J. Birgeneau, M. A. Kastner, M. Greven, and Y.-J. Kim, J. Phys. Soc. Jpn. **69**, 1170 (2000).

H. Hiraka, Y. Endoh, M. Fujita, Y. S. Lee, J. Kulda, I. A., and R. J. Birgeneau, J. Phys. Soc. Jpn. **70**, 853 (2001).

C. Stock, W. J. L. Buyers, Z. Yamani, C. L. Broholm, J.-H. Chung, Z. Tun, R. Liang, D. Bonn, W. N. Hardy, and R. J. Birgeneau, Physical Review B (Condensed Matter and Materials Physics) **73**, 100504 (2006).

C. Stock, R. A. Cowley, W. J. L. Buyers, R. Coldea, C. Broholm, C. D. Frost, R. J. Birgeneau, R. Liang, D. Bonn, and W. N. Hardy, Physical Review B (Condensed Matter and Materials Physics) **75**, 172510 (2007).

S. Shamoto, M. Sato, J. M. Tranquada, B. J. Sternlieb, and G. Shirane, Phys. Rev. B **48**, 13817 (1993).

A. T. Savici, I. A. Zaliznyak, G. D. Gu, and R. Erwin, Physical Review B (Condensed Matter and Materials Physics) **75**, 184443 (2007).

M. Fujita, H. Goka, K. Yamada, and M. Matsuda, Phys.Rev.B **66**, 184503 (2002c), URL `10.1103/PhysRevB.66.184503`.

K. Yamada, C. H. Lee, K. Kurahashi, J. Wada, S. Wakimoto, S. Ueki, H. Kimura, Y. Endoh, S. Hosoya, G. Shirane, et al., Phys. Rev. B **57**, 6165 (1998).

D. Poilblanc and T. M. Rice, Phys. Rev. B **39**, 9749 (1989).

J. Zaanen and O. Gunnarsson, Phys. Rev. B **40**, 7391 (1989).

J. M. Tranquada, D. J. Buttrey, and V. Sachan, Phys. Rev. B **54**, 12318 (1996).

H. Yoshizawa, T. Kakeshita, R. Kajimoto, T. Tanabe, T. Katsufuji, and Y. Tokura, Phys. Rev. B **61**, R854 (2000).

S. Wakimoto, G. Shirane, Y. Endoh, K. Hirota, S. Ueki, K. Yamada, R. J. Birgeneau, M. A. Kastner, Y. S. Lee, P. M. Gehring, et al., Phys. Rev. B **60**, R769 (1999).

W. Bao, Y. Chen, K. Yamada, A. T. Savici, P. L. Russo, J. E. Lorenzo, and J.-H. Chung, Physical Review B (Condensed Matter and Materials Physics) **76**, 180406 (2007).